P-wave velocities across the α - b quartz transition at lower continental crust pressure and temperature conditions

Arefeh MOAREFVAND[1], Julien Gasc[1], Damien Deldicque[1], Loic Labrousse[2], and Alexandre Schubnel[1]

[1]École Normale Supérieure, PSL
[2]UPMC

August 8, 2023

Abstract

The quartz α - b transition is a displacive phase transition associated with a significant change in elastic properties. However, the elastic properties of quartz at high-pressure and temperature remain poorly constrained experimentally, particularly within the field of β-quartz. Here, we conducted an experimental study on the quartz α - b transition during which P-wave velocities were measured in-situ at pressure (from 0.5 to 1.25 GPa) and temperature (200 to 900 °C) conditions of the continental lower crust. Experiments were carried out on samples of microcrystalline material (grain size of 3-6 μm) and single-crystals. In all these, the transition was observed as a minimum in P-wave velocities, preceded by an important softening, while P-wave velocities measured in the β-quartz field were systematically lower than that predicted by thermodynamic databases. Additional experiments during which acoustic emission (AE) were monitored showed no significant peak of AEs near or at the transition temperature. Microstructural analysis nevertheless revealed the importance of microcracking while Electron Back-Scatter Diffraction (EBSD) imaging on polycrystalline samples revealed a prevalence of Dauphiné twinning in samples that underwent through the transition. Our results suggest that the velocity change due to the transition known at low pressure might be less important at higher pressure, implying a change in the relative compressibilities of α and β quartz. If true, the velocity changes related to the α - b quartz transition at lower crustal conditions might be lower than that expected in thickened continental crust.

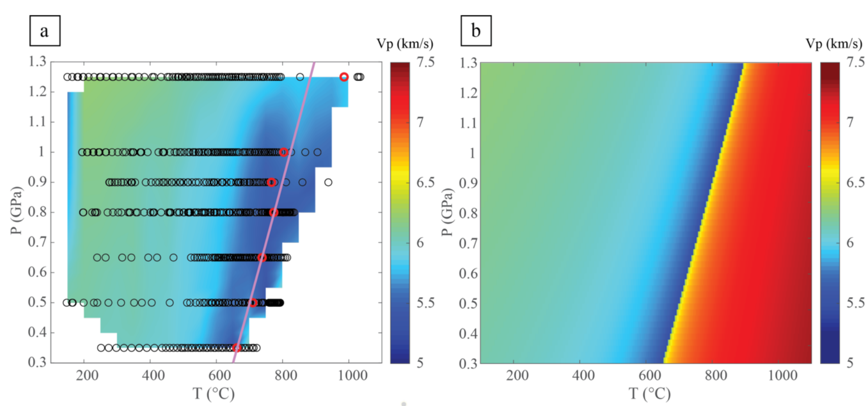

P-wave velocities across the $\alpha \rightarrow \beta$ quartz transition at lower continental crust pressure and temperature conditions

Arefeh Moarefvand[1] Julien Gasc[1] Damien Deldicque[1] Loic Labrousse[2] Alexandre Schubnel[1]

[1]Laboratoire de Géologie, École Normale Supérieure/CNRS UMR 8538, PSL University, Paris, France
[2]ISTEP, Sorbonne Université, Paris, France

Key Points:

- P-wave velocities measured in quartz at pressure and conditions of the continental lower crust
- $\alpha \rightarrow \beta$ quartz transition was observed as a minimum in P-wave velocities, preceded by important softening
- Our results suggest the velocity change due to the transition decreases with increasing pressure

Corresponding author: Arefeh Moarefvand, `arefeh.maaref@gmail.com`

Abstract

The quartz $\alpha \rightarrow \beta$ transition is a displacive phase transition associated with a significant change in elastic properties. However, the elastic properties of quartz at high-pressure and temperature remain poorly constrained experimentally, particularly within the field of β-quartz. Here, we conducted an experimental study on the quartz $\alpha \rightarrow \beta$ transition during which P-wave velocities were measured in-situ at pressure (from 0.5 to 1.25 GPa) and temperature (200 to 900 °C) conditions of the continental lower crust. Experiments were carried out on samples of microcrystalline material (grain size of 3-6 μm) and single-crystals. In all these, the transition was observed as a minimum in P-wave velocities, preceded by an important softening while P-wave velocities measured in the β-quartz field were systematically lower than that predicted by thermodynamic databases. Additional experiments during which acoustic emission (AE) were monitored showed no significant peak of AEs near or at the transition temperature. Microstructural analysis nevertheless revealed the importance of microcracking while Electron Back-Scatter Diffraction (EBSD) imaging on polycrystalline samples revealed a prevalence of Dauphiné twinning in samples that underwent through the transition. Our results suggest that the velocity change due to the transition known at low pressure might be less important at higher pressure, implying a change in the relative compressibilities of α and β quartz. If true, the velocity changes related to the $\alpha \rightarrow \beta$ quartz transition at lower crustal conditions might be lower than that expected in thickened continental crust.

Plain Language Summary

Phase transitions occurring in minerals at high pressures and temperatures can cause seismological discontinuities, and they happen when the mineral structure transforms from its stable form at lower pressures to a different structure at higher pressures and temperatures. One such transition that has a significant seismic signature is the alpha-beta quartz transition. Seismologists use this signature to determine the temperature conditions in the Earth's crust at depths much greater than those achievable in laboratory experiments. However, the uncertainty arises due to the fact that the alpha-beta quartz transition has only been observed under low-pressure conditions, and it is unclear whether it actually occurs at greater depths. In order to address this, we conducted a series of experiments at increasing confining pressures up to 1.25 GPa (equivalent to a depth of 35 km) and found that the transition becomes less sharp at high pressure. Our results suggest that the transition should not be as sharp as previously thought in seismological images at these depths.

1 Introduction

Trigonal α-quartz transforms to hexagonal β-quartz through a displacive polymorphic phase transformation. At atmospheric pressure, this transition occurs at 575 °C (Le Chatelier, 1890) and the transition temperature increases with pressure. The quartz $\alpha \rightarrow \beta$ transition has been detected in the laboratory up to 3 GPa by different experimental methods (Cohen & Klement Jr, 1967; Mirwald & Massonne, 1980; Van Groos & Heege, 1973; Shen et al., 1993; Bagdassarov & Delépine, 2004) and for single crystals, the Clapeyron slope of the transition is $\sim$ 0.25 K/MPa as reported by (Shen et al., 1993) using laser interferometry.

The $\alpha \rightarrow \beta$ quartz transition is also known for being a λ-transition (Dorogokupets, 1995; Angel et al., 2017), for which the behavior of the first derivatives in volume with respect to P (pressure) and T (temperature) makes it difficult to calculate the pressure and temperature dependence of thermodynamic properties. This arises from the impossibility to extrapolate thermodynamic functions of the low temperature phase (α) into the stability field of the high-temperature phase, and conversely it is impossible to extrapolate functions of the high-temperature phase (β) down to lower temperatures (Dorogokupets, 1995). Nevertheless, parameters used in most thermodynamic databases consist of extrapolations of low pressure experimental data. Berman (1988) introduces a λ-term in the expression of heat capacity C_p, fitted at low pressure for its dependence on T and assumed to be independent of P. Holland and Powell (1998) used the Landau formalism with a dependence in P. Abers and Hacker (2016) use a null thermal expansion coefficient for the β phase and extrapolate the fitting of low pressure K (isothermal bulk modulus) dependence on T at higher pressure, assuming dK/dP to be equal to 4 in the β field, in order to simplify the finite strain estimate used in the density and K calculations. Eventually, Dorogokupets (1995) elaborates a different approach, combining a quadratic T dependence on heat capacity and a derivative of thermal expansion depending on P and using the Murnaghan equation. Overall, all these extrapolations predict a drastic jump in K, and hence in P-wave velocities at the $\alpha \rightarrow \beta$ quartz transition.

Sharp velocity contrasts detected in the seismological record have been attributed to this expected jump at the $\alpha \rightarrow \beta$ quartz transition. In the southern Tuscany geothermal fields, a high amplitude seismic reflection between 3 and 9 km depth has been ascribed to the $\alpha \rightarrow \beta$ transition (Marini & Manzella, 2005; Zappone & Benson, 2013). Using the extrapolation of the transition temperature towards higher pressures, the $\alpha \rightarrow \beta$ quartz transition has also been used in several studies by seismologists to constrain the temperature profile of the lower crust. For instance, a significant increase in V_P/V_S at $\sim$ 50 km depth beneath southern Tibet has been interpreted as a result of the $\alpha \rightarrow \beta$ quartz transition by Sheehan et al. (2014). However, Kuo-Chen et al. (2012) observed V_P/V_S shallower anomalies at $\sim$ 24 km depth beneath Taiwan that they also ascribed to the $\alpha \rightarrow \beta$ quartz transition. Similarly, Mechie et al. (2004) observed a seismic discontinuity at 15 to 20 km deep under Tibet and interpreted it as the $\alpha \rightarrow \beta$ quartz transition.

Besides its seismological signature, the $\alpha \rightarrow \beta$ quartz transition itself has been considered as a potential weakening mechanism for the continental crust, due to the transient drop in elastic strength and the expected large thermal expansion in the vicinity of the transition (Mainprice & Casey, 1990; Johnson et al., 2021). The microcracking damage observed in experimental studies (Doncieux et al., 2008) have been considered as responsible for a drastic porosity change beyond the reaction in the Tuscany geothermal fields (Marini & Manzella, 2005; Zappone & Benson, 2013) and the residual stress left by the transition itself has been estimated as high enough to overcome rock strength and promote seismicity (Nikitin et al., 2006). This transition is therefore expected to have a dramatic effect on quartz-bearing crustal rocks through the whole crustal temperature range, if the properties deduced from low pressure experiments are still valid at higher pressure.

At low pressures, the $\alpha \rightarrow \beta$ transition is accompanied by significant changes in elastic properties (Ohno, 1995; Carpenter et al., 1998; Ohno et al., 2006). In apparent contradiction to Birch's law (Birch, 1960, 1961) which states that elastic wave velocities should evolve linearly with density, the transition is accompanied by an increase in wave velocities in the (lower density - high temperature) β-quartz. Maximum P and S wave velocities for quartz aggregate change from 5.95 to 6.4 km/s and from 4 to 3.9 km/s, respectively (Kern, 1979), while P-wave velocity anisotropy actually decreases from 50% in the α field to 15 % in the β field (Gibert & Mainprice, 2009). However and to the best of our knowledge, the effect of the $\alpha \rightarrow \beta$ quartz transition on the elastic wave velocities in quartz has only been investigated by two distinct laboratory studies under pressure, and only up to 0.4 GPa. Using ultrasonic methods, seismic wave velocities have been measured across the transition by Kern (1979) on quartz single crystals, pure quartzite, granite ($\sim$ 21% Qz) and granulite ($\sim$ 28% Qz) samples at 0.2 and 0.4 GPa confining pressure. Zappone and Benson (2013) measured the P-wave velocity across the transition on a micaschist sample, with 36% of quartz, at 0.2, 0.3 and 0.4 GPa confining pressure. Both studies have reported an important decrease of seismic velocities prior to the transition and a sudden increase - yet generally lower than that predicted by the thermodynamic databases - of P-wave velocities once in the field of β-quartz. Both studies observe minimum in elastic wave-velocities at P-T conditions compatible with the occurrence of the transition. Yet, Kern (1979) also observed an apparent higher transition temperature for granite and granulite, when compared to quartzite and quartz single crystals at the same pressure conditions.

In summary, and despite more than a hundred years of studies, the elastic properties of quartz at high pressure remain poorly known, particularly within the β quartz field. Here, using a new set-up (Moarefvand et al., 2021), we document *in situ* the evolution of P-wave velocities of quartz aggregates and single crystals, duringtemperature crossing of the $\alpha \rightarrow \beta$ quartz transition at pressures ranging from 0.35 to 1.25 GPa. Additional experiments were performed using acoustic emission recording as a probe to study the occurrence of microcracking during the transition. Microstructures within our recovered samples were also investigated using Scanning Electron Microscopy (SEM) and Electron Back Scattered Diffraction (EBSD).

2 Materials and Methods

In the following section, we describe the sample preparation and assembly, the experimental set-up and methods, all previously presented by Moarefvand et al. (2021).

2.1 Sample preparation

Our starting material consisted of hard translucent Arkansas novaculite, purchased from a whetstone company based in Arkansas, USA. Novaculite is a dense, hard, fine-grained sedimentary rock, composed of more than 99 percent pure silica. The origin of silica is biogenic, consisting primarily of siliceous skeletal particles of marine organisms such as sponge spicules and radiolaria, and very fine-grained, wind-blown quartz particles. The grains measure between 3 and 6 μm and the initial porosity is below detection threshold. The starting material has been analyzed using EBSD and no crystal preferred orientation has been observed. Four experiments were also performed on a quartz single crystal (of unknown origin), in order to compare the results with those of the microcrystalline novaculite and document the change in V_p anisotropy through the transition at high pressure.

In both cases, cylindrical specimens were cored and manually polished to ensure maximum parallelism of both end-surfaces. Samples were cylinders of 4.5 mm in diameter and 10 mm in length. The exact sample length was measured before each experiment (Table 1). For the single crystal, cores were made either parallel or perpendicular to the c-axis. The sample was then encapsulated in a gold or platinum jacket (0.25 mm wall thickness) and placed at the center of the solid-medium cell assembly (Figure 1.a), where it is surrounded by cold-pressed fine-grained salt pieces, used as confining medium. A graphite furnace, sleeved by two pieces of hard-fired pyrophyllite, is used for heating and two thermocouples measure the temperature inside the assembly. More details on the sample assembly can be found in Moarefvand et al. (2021). After each experiment, the samples was embedded in epoxy and cut along its long axis. Sections were then polished with polishing cloths and diamond paste of decreasing grain size until 0.25 μm and finally, with 0.05 μm colloidal silica, to obtain a highly reflective surface suitable for Electron Back-Scattered Diffraction (EBSD) analysis.

2.2 Experimental set-up

Experiments were performed using the newly installed third-generation Griggs apparatus at the Laboratoire de Géologie of École Normale Supérieure Paris, designed to perform deformation experiments at P-T conditions up to 5 GPa and 1000 °C. This apparatus is a modified piston cylinder apparatus used to generate a controlled environment of high pressure, high temperature and deviatoric stress. At the core of this apparatus lies the 20 mm diameter solid-medium sample assembly (Figure 1.a). Axial load (σ_1) is applied via a series of alumina and tungsten carbide (WC) pistons of 5 mm diameter, above the specimen. The confining pressure (σ_3) is transmitted via a cylindrical WC piston of 20 mm in diameter to the cell assembly (Figure 1.a and b). Confining and differential stresses are driven via two servo-controlled high pressure precision micro-volumetric pumps and during the experiments, a set of three LVDTs (Linear Variable Differential Transducers) allows us to measure the relative displacement of the confining and differential stress pistons. The stiffness of the apparatus was calibrated and found to be 20 μm/kN. Temperature gradients inside the cell assembly were also previously assessed by Moarefvand et al. (2021).

In this study, all experiments were carried out at constant confining pressure, maintaining the conditions as close as possible to hydrostatic (no measurable differential stress). Experiments were performed at pressures ranging from 0.35 to 1.25 GPa. The pressure was first slowly raised under moderate temperature conditions (typically 100-200 °C). Once the target pressure was reached, the temperature was increased at a rate of 10 °C/ min, from 200 to 1000 °C (above the transition temperature), and then quenched. To compensate for thermal pressure during the ramping of temperature, the confining pressure was maintained constant and the differential stress close to zero by enabling both the confining and differential stress pistons to slowly retract, using the servo-controlled pumps in constant pressure mode. The thermal expansion of the axial (σ_1) column was measured this way and found to be 1μm/K. Parameters recorded every second during the experiment include displacements ($\pm$0.1 μm), axial (σ_1) and confining (σ_3) stresses ($\pm$ 0.05 GPa) and temperature ($\pm$ 20 °C). More details on the experimental set-up and calibration procedures can be found in Moarefvand et al. (2021).

2.3 Active and passive acoustic monitoring set-up

Two high-frequency (5-10 MHz) industrial piezoelectric transducers were used for active acoustic monitoring to measure P-wave velocities during the experiment. The bottom transducer (Olympus V110, P-wave, 5 MHz center frequency) is located below the sample assembly, glued directly under the baseplate (Figure 1.b). The bottom transducer, used as the ultrasonic source, is connected to a software-controlled pulse-box custom-made by Eurosonics/Mistras. Electric impulses of 250 V , 0.1 μs long, are sent at 1kHz repetition rate to the bottom transducer, which converts these electric pulses into planar guided P-waves propagating along the deformation column. The top transducer (Olympus V129, P-wave, 10 MHz center frequency) is located above the sample assembly, glued on a tungsten carbide (WC) spacer placed within the deformation column. The top transducer, used as the ultrasonic receiver, is amplified at 38 dB. Note that a 5-10MHz frequency corresponds, for a P-wave velocity of 5 km/s, to 0.5-1 mm wavelength, i.e. 10 to 20 times smaller than the sample's length.

To increase the signal-to-noise ratio, stacks of 1000 waveforms, synchronized by the pulse box, were recorded every minute during the experiment. Stacked waveforms are collected with a sampling frequency of 50 MHz. A typical stacked waveform recorded by the top transducer during an experiment is represented on figure 2.b, where t_o and t_p represent the time of pulsing and the arrival time of the P-wave on the top transducer, respectively, $(t_p - t_o)$ thus representing the travel time between both transducers. The acoustic stiffness, i.e., the travel time delay due to the shortening of the column upon axial loading (3 ns/kN), and temperature dependence (0.4 ns/K) of the travel time through the column were also calibrated, discussed and interpreted by Moarefvand et al. (2021).

To record acoustic emissions, an S-wave transducer (Olympus V156, 5 MHz center frequency) was used instead as bottom transducer (Fig. 2.a). The S-wave transducer being sensitive to both S and P waves, the arrival time difference $(t_p - t_s)$ of both waves can be used as a proxy for 1D localization along the column. AEs are detected using a 60 db amplifications and a simple threshold logic. Whenever the threshold is crossed, waveforms are collected at a 50MHz sampling frequency and the signal is recorded both non-amplified and amplified (at 30 dB and 60 dB). Gasc et al. (2022) have demonstrated that the AE system is sensitive to the propagation of cracks ranging from a few tens of μm to a few mm in size. One example of recorded waveforms is illustrated on figure 2.c.

2.4 Data processing and P-wave velocity measurements

P-wave arrival times and time-differences are determined using a cross correlation (CCR) algorithm in reference to a master waveform, which is manually picked. Prior to the CCR, waveforms are resampled at 100 MHz using a spline interpolation function, so that the resolution of the measured time-differences is of the order of 10 ns. This pre-processing of the acoustic data is performed using the software Insite (Applied Seismology Consulting). The PZT transducers are not directly in contact with the sample (figure 2.a) and most of the travel time actually occurs along the axial column between the two transducers. The travel time through the column, and its pressure and temperature dependencies, therefore need to be precisely calibrated in order to calculate the P-wave velocity V_p in from the travel time knowing the sample's length.

At any given time during the experiment, we have $t(P,T) = t_s(P,T) + t_c(P,T)$, with $t(P,T)$, $t_s(P,T)$ and $t_c(P,T)$ respectively the measured travel time, the travel time in the sample and travel time in the column. To estimate the initial quartz velocities and their theoretical evolution during the experiments, we use the (Abers & Hacker, 2016) MATLAB® toolbox, which calculates elastic moduli and density of crystals at high pressure and temperature using a database of thermodynamic parameters of 60 minerals. Using this toolbox, we calculate the velocity V_o of α quartz at a reference pressure (0.5 GPa) and temperature (350 °C). Knowing the sample length $L(P,T)$ at this reference temperature and pressure during an experiment on novaculite, we calculate the travel time in the sample $t_s(0.5, 350) = L(0.5, 350)/V_o$. We can then calculate the travel time in the column at 0.5 GPa and 350 °C:

$$t_c(0.5, 350) = t(0.5, 350) - t_s(0.5, 350)$$

Changes in column length due to elastic loading and thermal expansion were determined from deformation and heating calibration experiments, from which both the temperature ($\beta = 0.4ns/K$) and pressure ($k_a = 3ns/kN$) dependencies of the travel time in the column were obtained (Moarefvand et al., 2021). Using the above, we may calculate the travel time in the column at any given P-T conditions:

$$t_c(P,T) = t_c(0.5, 350) - \beta(T - 350) - k_a S_o(P_o - P)$$

where S_o is the sample section area $S_o = \pi r^2$, which is fixed as constant and equal to r = 4.5 mm. Finally, we obtain the P-wave velocity within the sample at any (P,T) by correcting for the travel-time in the column:

$$V_p(P,T) = \frac{L(P,T)}{t_s(P,T)} = \frac{L(P,T)}{t(P,T) - t_c(P,T)}$$

Since t_c can be calculated at given P and T, this method allows us to retrieve P-wave velocities during all of our experiments, using a single reference point at 0.5 GPa and 350 °C, the length of the sample and its evolution during the experiment, $L(P,T)$ being determined independently with the use of an LVDT.

The measured V_p at 0.5 GPa confining pressure (blue curve on Figure 3), when corrected for temperature effects on the travel time through the column (yellow curve on Figure 3) compares remarkably well to the Abers and Hacker (2016) prediction at these experimental conditions (solid gray curve on Figure 3).

Note that all three curves intersect at 0.5 GPa and 350 °C due to the calibration procedure described above. In the following, we chose to correct all travel times for temperature effects and use only one anchorage point at 350 °C/0.5 GPa for all curves (red dot on figure 3) including for quartz single-crystals, so that possible pressure effects are not due to or hidden by calibration artefacts. The actual error bar on these measurements is hard to assess, but we expect an error of $< 10\%$ on corrected velocities, due to small changes in column length between experiments, and a resolution of $\sim 0.1km/s$ between relative measurements performed within a single experiment.

3 Experimental results

A total of 14 experiments (Table 1) were performed at high pressure and temperature. Experimental conditions and results are summarized in Table 1. Initial and final length of the samples were measured systematically, and in most cases, final shortening was maintained $< 5\%$.

3.1 P-wave velocities evolution during $\alpha \rightarrow \beta$ quartz transition in novaculite at high-pressure

The evolution of P-wave velocities measured on novaculite samples versus temperature are displayed on Figure 4. For all experiments, the P-wave velocity decreases gradually with the temperature and reaches a minimum value, beyond which an abrupt rise is observed. The temperature corresponding to the minimum in velocity is interpreted as being the $\alpha \rightarrow \beta$ quartz transition temperature. As expected, this minimum value in velocity progressively shifts to higher temperatures with increasing confining pressure. Whatever the pressure, the gradual velocity decrease observed in the α-quartz field prior to the transition is almost fully recovered once at high temperature in the β-quartz field. A trend of increasing velocity with increasing pressure is observed in the α-field. At low pressure (0.35 and 0.5 GPa), the maximum values of V_p measured in the β-field are, as expected, higher than those measured at low temperature in α-quartz. However, during the highest pressure experiments, our measures of P-wave velocities within the β-field were limited by the melting point temperature of the confining medium (halite). Once reached, molten salt started to convect, which, changing the radial temperature gradients within the assembly, induced an uncontrolled increase of the temperature in the sample.

Two additional experiments were carried out at 0.5 and 0.8 GPa confining pressure on novaculite using the AE recording set-up, in order to study the mechanical effect of the $\alpha \rightarrow \beta$ transition. Figure 5 compares AE recording experiments with experiments conducted at the same P-T conditions, during which P-wave velocities were measured (nb: unfortunately, our current system does not allow doing both concurrently). Below 400 °C, dozens of AEs were detected upon heating. Note that this low temperature burst of AEs is not accompanied by a sharp decrease in velocities, in such a way that the cracks at the source of the AEs do not seem to affect much the elastic properties of the sample. On the contrary, above 400 °C, while the P-wave velocity softening is strongest, hardly any AEs were detected. At 0.5 GPa, the transition itself is not associated with a detectable burst of AEs. At 0.8 GPa, a burst of AEs was detected close to the transition. Note that this burst is smaller than what was detected at temperatures below 400 °C. From this, we may conclude that there is no significant dynamic microcracking effect during the quartz $\alpha \rightarrow \beta$ transition at high-pressure under hydrostatic stress. However, one should keep in mind that if microcrack propagation is slow (or quasi-static), it can remain unnoticed because of the inherent limitations in the AE detection capability of our system.

3.2 P-wave velocities evolution during the $\alpha \rightarrow \beta$ quartz transition in quartz single-crystals at high-pressure

In order to isolate the possible effect of grain boundaries and intergrain interactions from intra-crysatlline processes on the transition and the evolution of seismic anisotropy through the latter, four additional experiments were carried out on quartz single-crystals. Two samples were cored parallel to the c-axis, and two normal to the c-axis. Experimental conditions and transition temperatures $T_{\alpha \rightarrow \beta}$ are given in Table 1. The evolution of P-wave velocity during these experiments at 0.5 and 0.8 GPa are presented in Figure 6. The P-wave anisotropy of quartz is larger at higher pressure, from a value of $(V_c - V_a)$ of 0.55 km/s at 0.5 GPa and 350 °C to 1.2 km/s at 0.8 GPa and 350 °C. The evolution of P-wave velocities measured in novaculite at the same pressures lies between the ones measured along the slow and fast directions in single crystals, consistently with the random orientation of quartz crystals in novaculite.

The softening prior to the transition, and the subsequent recovery at high temperature, is larger for waves propagating along the c-axis. The P-wave velocities measured in novaculite in the α-quartz field at 0.5 GPa are well-matched by the Abers and Hacker (2016) prediction. The match between the theoretical prediction and our data is not as good at 0.8 GPa, although the amount by which V_p decreases until the transition temperature in our data is also remarkably similar to what is predicted by Abers and Hacker's database. Finally, note that the minimum in P-wave velocity is reached at lower temperatures for single-crystals than for the microcrystalline aggregate at the same pressure (Table 1 and Fig. 6). This difference, also observed by Kern (1979), could either be due to the anisotropy of thermal expansion and compressibility of quartz and/or the pervasive opening of grain boundaries in the microcrystalline aggregates delaying the apparent rise of velocity beyond the transition temperature in novaculite experiments.

3.3 Microstructural analysis

Samples were first imaged in reflected optical light using a digital microscope with a magnification of 200x (Figures 7 and 8). Images of single-crystal samples (Figure 7) demonstrate our samples did not undergo significant shortening (or deformation) as no shear cracks with visible offset can be observed at the sample scale, thus demonstrating the samples underwent the transition in conditions relatively close to hydrostatic. Yet, horizontal and vertical cracks are pervasive and dissect the initial crystals. Microcracking seems to have been more intense at lower pressure (0.5 GPa) and parallel to the c-axis, which may be due to the anisotropic thermal expansion of quartz. Nevertheless, it is impossible to conclude whether the propagation of these microcracks took place at high pressure and temperature conditions, or rather, upon quenching and decompression.

Images of novaculite samples (Figure 8) show no significant shortening, except in $NA_{0.5}$ and $NA_{0.8}$ where shear fractures accompanied by tangential displacement are visible in the lower part of images. Associated shortening is lower than $\sim$ 7%. Yet, fractures without tangential displacement are visible in all samples. Horizontal fractures are interpreted as decompression cracks. The set of vertical cracks, observed in all samples except $NA_{0.65}$ is more intriguing. No apparent displacement is associated to them (mode I). They may have been produced at high pressure and temperature conditions, but they are absent in $NA_{0.65}$) and confining pressure seems to have little effect on their propagation. In any case, quenching and pressure unloading of the sample causes significant transient deviatoric stress, likely responsible for these brittle features, as suggested by the numerous acoustic emissions (AE) recorded in this final step of the experiments.

To complement our microstructural analysis, EBSD maps were acquired on several zones on selected samples, with a step size of 0.5 μm (Figure 9 and Table 2). EBSD maps were then analyzed using the MTEX matlab toolbox (Bachmann et al., 2010), which allows determining grain-boundaries, grain size and shape parameters. Grain boundaries were identified using a misorientation threshold of 13° between neighboring pixels. The results of EBSD analysis of the starting novaculite and our HP-HT samples is summarized in Table 2. In addition, we also analyzed a sample that did not cross the transition, yet underwent 1 GPa of pressure and moderate temperature (700 °C) (NA_1^*). The average grain-size of the starting novaculite is 5.51 μm. Samples that experienced HP-HT conditions present a slight grain-size reduction, with a final grain-size ranging between 3.39 and 4.43 μm, and a slight increase in the grain aspect ratio (Table 2).

We also searched for evidence of Dauphiné twinning, which result in a 60° rotation of the a-axis around the c-axis. Previous studies have shown that the structure of $\beta-$quartz can be described geometrically as a spatial average of two Dauphiné twin configurations (Heaney & Veblen, 1991) and Dauphiné twinning have thus been used as a marker of former $\alpha \rightarrow \beta$ transition in rocks that underwent the $\alpha \rightarrow \beta$ transition (Wenk et al., 2009). Here, we used the ratio between the cumulative twin boundary length to total grain boundary length as a proxy for the amount of Dauphiné twinning. The starting material has a ratio of 0.48%, while samples that underwent the $\alpha \rightarrow \beta$ transition have ratios ranging between 6.3 and 19%. Dauphiné twinning is therefore not inherited from starting material and developed during experiments. Sample NA_1^*, which did not undergo the transition, exhibits a mean twinning ratio of 8% (see Table 2), implying that some Dauphiné twinning also occurred in the α-field. Three of the experiments show a twinning ratio significantly larger or equal to the ratio observed in sample NA_1^*, while the other two show similar values. Sample $NA_{1.25}$ has been extensively mapped to detect any internal heterogeneity in the twinning ratio pattern. Ratio remains fairly uniform throughout sample, except for a small region in the bottom center part, where higher temperatures may have contributed to an increase in twinning ratio (Moarefvand et al., 2021). Dauphiné twinning is also concentrated along cracks, possibly due to higher stress concentrations at the grain boundary scale caused by strain incompatibilities.

4 Discussion

4.1 Microstructural evidence of the transition

Because of the displacive nature of the transition, β-quartz cannot be quenched. In consequence, only a few microstructural arguments exist that may evidence that quartz crystals actually underwent the transition. Among these, microcracking and the occurrence of Dauphiné twins are the most prominent (Johnson et al., 2021; Wenk et al., 2009). Quantitative microstructural data on samples that experienced the transition at high-pressure are still lacking. At atmospheric pressure, laboratory studies have reported microcracking associated to the transition using micro-indentation or acoustic emission (AE) techniques (Darot et al., 1985; Schmidt-Mumm, 1991; Glover et al., 1995; Meredith et al., 2001). Doncieux et al. (2008) demonstrated the irreversibility of crack damage, as only a reduced number of AEs were detected when the temperature was lowered across the reversed ($\beta \rightarrow \alpha$) transition. The $\alpha \rightarrow \beta$ quartz transition being a λ-transition, the occurrence of damage could be explained by the important rise of thermal expansion of α-quartz near the transition (Kern, 1979). Another interpretation is the reduction of the Griffith fracture energy criterion to nearly zero at the transition, as observed by Darot et al. (1985). Here, our postmortem analysis also revealed pervasive mode-I microcracking, although it is difficult to infer whether this microcracking took place at high pressure and temperature conditions or not. In that sense, AE monitoring did reveal that if microcracking took place at high pressure and temperature, it propagated in a quasi-static manner (absence of major AE bursts at or around the transition temperature).

Dauphiné twinning density in experimental products having crossed the $\alpha \rightarrow \beta$ transition is significantly higher than in the reference sample that remained in the α-field. Two experiments, $NA_{1.25}$ and $NA_{0.65}$, showing a P-wave velocity curve symptomatic of the $\alpha \rightarrow \beta$ transition, nevertheless exhibit a low Dauphiné twinning density. The transition therefore does not systematically leave Dauphiné twins behind. Experiment $NA_{0.65}$ is the one with the shortest residence time in the β-field, and experiment $NA_{1.25}$ is the one with the smallest difference between maximum temperature reached and transition temperature (Figure 4). These specificities might explain their lower twin densities. In addition, Dauphiné twins can also result from deviatoric stress (Minor et al., 2018; McGinn et al., 2020). The significance of the Dauphiné twins thus remains a question. Dauphiné twins could either constitute a remnant of the incomplete transformation of α quartz into β, which was imaged under TEM as the growth of Dauphiné twin domains (Heaney & Veblen, 1991) or twins could also emerge as a response to deviatoric stresses caused by strain incompatibilities during the transformation. The differential stress threshold for Dauphiné twinning in quartz aggregates is approximately 50 MPa, which falls well within the uncertainty range of the stresses applied within ab the Griggs apparatus (Moarefvand et al., 2021; Holyoke III & Kronenberg, 2010; Wenk et al., 2006). Unsought deviatoric stress might have developed in some experiments and caused some of the twinning observed. Our sample NA_1^* that did not cross the transition shows a twin density comparable to that of two samples that did ($NA_{0.65}$ and $NA_{1.25}$). These two later experiments show evidences for very low deviatoric stresses, with a very well-preserved sample shape (Figure 8). It is therefore possible that these two experiments, did not develop internal stresses high enough to activate Dauphiné twinning or preserve twins during cooling. These observations, as well as the higher twin density near the most deformed parts of the samples, nevertheless suggest that both the $\alpha \rightarrow \beta$ transition and deviatoric stress can induce the appearance of significant Dauphiné twins (figure 10). The highest twin densities measured here are likely caused by a combination of both mechanisms.

4.2 Comparison with previous experimental data and thermodynamic databases

Our experimental P-wave velocity measurements on quartz single crystals can be compared with those of Kern (1979), performed at 0.2 and 0.4 GPa (Figure 11). In quartz single-crystals, P-wave velocities are faster along the c-axis ($V_{\parallel c}$) at all pressure conditions, in agreement with Kern (1979). $V_{\parallel c}$ also show a positive pressure dependence of $\sim 1.2km/s/GPa$ within the 0.2-0.8 GPa range. However, and in contradiction with the observations of Kern (1979), we observe a negative pressure dependence of the P-wave velocities measured along the a-xis ($V_{\perp c}$) between 0.5 and 0.8GPa, which needs to be experimentally confirmed and reproduced. We observe that the temperature softening before the transition, also observed in Novaculite, is much less pronounced for P-wave velocities propagating along the a-axis than along the c-axis. The velocity jump once in the $\beta-$ field is also more pronounced for $V_{\parallel c}$ than for $V_{\perp c}$. These differences result in significant variations in P-wave anisotropy ($V_{\parallel c}/V_{\perp c}$) across the temperature range investigated. We observe that the anisotropy decreases quasi-linearly when approaching the transition temperature, and increases sharply once in the $\beta-$ quartz field. This late increase in anisotropy has not been observed by Kern (1979) due to the scarcity of data points within the $\beta-$ field. It is nevertheless expected from extrapolations of quartz elastic properties at high temperatures (Mainprice & Casey, 1990).

Experimental P-wave measurements can be interpolated on a P-T diagram for comparison with the thermodynamic predictions using Abers and Hacker (2016) database (Figure 12). Except for experiment $NA_{1.25}$ that yields a minimum P-wave velocity 100 °C higher than expected, the P-wave velocity minimum observed experimentally (red circles on Figure 12) lies between 4 and 35 °C away from the $\alpha \rightarrow \beta$ transition pressure and temperature conditions determined by Shen et al. (1993) using laser interferometry. Considering a ± 25 °C uncertainty on our thermocouple measurement, the 5 experiments performed from 0.35 to 1.0 GPa show a minimum velocity at the expected temperature. $NA_{1.25}$ might suffer from overestimated temperature due to the proximity of melting temperature for halite at high pressure. In this latter experiment, unintentionally large temperature steps of 60 °C and 130 °C were performed for the last two heating steps within the α-field, while previous heating steps with equal heating power increment induced increments of about 10 °C only.

4.3 Velocities in the β-quartz field and possible experimental artefacts

Thermodynamic models generally account for the change of elastic properties at quartz $\alpha \rightarrow \beta$ transition, by propagating the elastic moduli measured at low pressure to high pressure (Angel et al., 2017; Abers & Hacker, 2016). In particular, Abers and Hacker (2016) use a null thermal expansion coefficient for the β-phase and extrapolate the fitting of low pressure K (isothermal bulk modulus) dependence on T at higher pressure, assuming dK/dP

to be equal to 4 in both the α- and the β- field. Consequently, the velocity jump they predict across the transition is unaffected by pressure change. P-wave velocities measured within α-field are in agreement with the ones predicted by Abers and Hacker (2016). However, our results seem to suggest that the amplitude of the increase in V_p through the $\alpha \rightarrow \beta$ transition decreases at increasing pressure. In the following, we discuss three possible causes for this discrepancy and the unexpected moderate velocities observed in the β-field: - transformation-induced cracks that might reduce V_p; ii- temperature gradients in the samples that could result in a progressive sample transformation; iii- potential errors when extrapolating the elastic parameters of β-quartz from low to high pressure, as already mentioned above.

Transformation-induced cracking

Cracking/fracturing at the transition temperature could modify the effective elastic behaviour at high pressure. At atmospheric pressure, experimental studies exhibit a peak of AEs at transition temperature (Schmidt-Mumm, 1991; Glover et al., 1995; Meredith et al., 2001). As previously discussed, no peak of acoustic emission has been observed near the transition temperature at 0.5 and 0.8 GPa on novaculite (Figure 5) which evidences that no major cracking affected our measurements. Although thermal expansion of quartz is anisotropic and varies through the $\alpha \rightarrow \beta$ phase transition, hence building up significant stress at grain boundaries, this effect is expected to be insignificant for grain sizes below 5 μm (McKnight et al., 2008). In addition, large pressure also should prevent mode-I cracking. So, both experimental results and mechanical considerations tend to discard this hypothetical artefact as a possible cause for the low velocities measured in the β-field.

Effects of temperature gradients

At room pressure, former studies have shown that the $\alpha \rightarrow \beta$ transformation occurs within a narrow temperature interval of < 1 °C. Considering that important temperature gradients are expected in our samples at high P-T (Moarefvand et al., 2021), the coexistence of the α and β phases is therefore likely over a temperature interval reflecting the range of temperature gradients, which, in turn, may explain why the present data does not exhibit a sharp velocity jump in the β-field with increasing temperature, but rather a steep continuous rebound. However, temperature gradients within the sample are estimated to be at most of a few tens of degrees (Moarefvand et al., 2021). These gradients alone can therefore not explain the low velocities obtained in the β)field, particularly in experiments $NA_{0.5}$and $NA_{0.8}$, where a good control on the temperature was kept far within the β-field ($\sim$100 °C), thus promoting full sample transformation. Temperature gradients inside the assembly lead, however, to transient mixed bulk elastic properties between untransformed low-velocity α domains and hotter transformed high-velocity β domains.

In order to evaluate the possible effect of temperature gradients, we modelled the evolution of P -wave velocities with Abers and Hacker (2016), considering a temperature gradient of - 50, - 100 and - 200 °C inside the sample assembly (Figure 14). A larger temperature gradient is expected to result in a less steep velocity change in both the α- and the β- quartz field (Figure 14). The slope of the velocity-temperature curve in the β- field from our experiment compares well with the increase computed for samples submitted to a gradient of 50-100 °C. On the other hand, the magnitude of the velocity decrease observed in the α- field is in agreement with (Abers & Hacker, 2016) predictions, which either suggests a negligible impact of temperature gradients in our samples, or reflects the gradual development of temperature gradients upon heating. Indeed, temperature gradients would lessen the decrease in velocity observed in the α-field, which is not observed. Nevertheless, heterogeneous transition within the sample would also imply heterogeneous transformational stress build-up, and hence heterogeneous Dauphiné twinning density. EBSD maps collected at the top versus that at the bottom, or at the core versus at the outer part of our samples, did not reveal any significant difference, suggesting that the transformation rate was rather homogeneous throughout each sample. Even though experimental artefacts might explain the observed limited velocity rise in the β-field, Johnson et al. (2021) numerical simulations show that the $\alpha \rightarrow \beta$ phase transition propagates due to heterogeneous stress distribution and quartz-grain orientations. Such a propagation mechanism over the timescale of our experiments cannot be excluded. However, no propagation pattern is observed in our EBSD maps (Fig. 9). Even the larger ones (up to 0.03 mm^2, figure 9) show homogeneous and isotropic twinning boundaries distributions, suggesting that, if occurring, this propagation was complete at peak temperatures. In summary, temperature gradients might well explain why the rise in velocity is less steep than predicted, but not why maximum velocities remain lower than that expected in the β-field.

Uncertainties regarding the elastic propoerties of β-quartz

Amongst the different equations of states or thermodynamic databases of quartz published in the literature, only the formalism of Dorogokupets (1995) predicts a decrease of the velocity rise within β-quartz with increasing pressure. Dorogokupets (1995) formalism also predicts that the λ-shaped anomaly spreads with increasing pressure and hence that the transition may become imperceptible at "some pressure", which is consistent with the imperceptible change in slope of the quartz-coesite transition at the intersection with the $\alpha \rightarrow \beta$ transition. This equation of state also implies that dK/dP is not constant in the β-field, and that it could even reach negative values at high pressures. Even though the actual physical meaning of a negative dK/dP remains unclear (at least to the authors of this manuscript), the comparison of our experimental results with V_p curves calculated with different dK/dP values using the (Abers & Hacker, 2016) formalism (Figure 14) suggests that this parameter might be indeed overestimated in most databases. For instance, using molar volume measurements, Lider and Yurtseven (2014) have calculated the isothermal compressibility of β-quartz as a quadratic function of P: $\kappa(P) = \kappa_o + \kappa_1 * P + \kappa_2 * P^2$, where κ_o and $\kappa(P)$ are the compressibilities of β-quartz at room pressure and at a given pressure, respectively. Using their coefficients ($\kappa_o = 0.035\ GPa^{-1}$; $\kappa_1 = -9.01 * 10^{-4}\ GPa^{-2}$; $\kappa_2 = -8.9 * 10^{-5}\ GPa^{-3}$) yields a bulk modulus of β quartz at room pressure and 1 GPa (and 878K) equal to 28.57 GPa and 29.4 GPa respectively, i.e. a dK/dP of ~ 0.8 only (close to the green dashed line in Figure 13).

5 Conclusions

We have investigated the α-β quartz transition at high pressure by measuring P-wave velocity with increasing temperature across the transition, at 0.35-1.25 GPa on both polycrystalline aggregates and single crystals. We observed a minimum in P-wave velocity at temperatures compatible with the predicted P-T conditions of the transition. The transition seems to occur at lower temperatures for single crystals than for the aggregates, which confirms an experimental observation by Kern (1978, 1979). We observe an increase in P-wave anisotropy with increasing pressure, P-wave velocities propagating 10-20% faster along the c-axis. P-wave anisotropy also decreases with increasing temperature in the α-quartz domain, and increases once in the β-quartz field.

Below the transition temperature, the expected softening, resulting in an important drop of the P-wave velocities, is well observed and matches the thermodynamic predictions. However, the increase of P-wave velocity within the β-quartz is smaller than predicted by thermodynamic databases (Figure 12), which is partly due, here, to the difficulties in investigating high temperatures with the use of NaCl as a pressure medium. Nevertheless, it is clearly observed that with increasing pressure, the velocity rise in the β-field becomes lower. Two experimental biases that can potentially explain this unexpected behavior were assessed: possible cracking through the transition and temperature gradients in the sample.

Acoustic emission monitoring revealed that there is no (dynamic) micro-cracking related to the transition, at least within the microcrystalline aggregate. Temperature gradients in the sample lead to gradual transformation of the sample, which explains the smoothing of the dip of the velocity-temperature curves at the transition compared to what is predicted by thermodynamics. However, the evolution of velocities in the α-quartz field compares very well with modelled velocity curves, which suggests a modest effect of thermal gradients on the transition. Whether or not these gradients remain small enough to allow full transformation beyond the minimum in velocity observed remains unclear. In other words, it is difficult to demonstrate that the highest velocity values obtained in the β-field actually do correspond to the maxima predicted by thermodynamics, which are supposed to be larger.

Dauphiné twins formed in all samples that underwent the $\alpha \rightarrow \beta$ transition and their homogeneous distribution across at least one of the samples points towards a full sample transformation. However, two samples show a twinning ratio comparable to that of the reference sample that remained in the α-quartz field (Table 2). It is therefore not possible to attribute all the twins to the transformation, and the respective contributions of grain-scale deviatoric stresses versus α-β transformation in producing Dauphiné twins remains to be determined.

Nevertheless, the increase of velocities obtained in the β-field becomes weaker with increasing pressure, which reveals that the bulk modulus of β-quartz and its pressure derivative remain largely unconstrained, and suggest that both K_o and K' are smaller than predicted by current thermodynamic databases. Consequently, the seismic anomaly related to the α-β quartz transition at high pressure might be smaller than predicted by these databases, which should thus be used with caution. Quartz grain size and orientation both can affect the transition temperature, and the elastic properties change due to the transition. In consequence, high pressure and temperature estimates of elastic parameters are still needed to improve the thermodynamic modelling of quartz, particularly within the β-quartz domain.

Finally, since the transition is expected to be smoother than currently computed, the above also implies a refinement of the interpretation of seismic discontinuities in terms of 'seismic signature' of the $\alpha \rightarrow \beta$ transition. While the K-horizon reflector documented in the Tuscany geothermal fields (Marini & Manzella, 2005) is shallow enough (9 km maximum, i.e. $\sim$ 0.3 GPa) to be directly due to the transition itself, the deeper reflectors at 15-20 km (ie 0.5 - 0.7 GPa) beneath Tibet (Mechie et al., 2004) or at 24 km (0.8 GPa) beneath Taïwan (Kuo-Chen et al., 2012) or even 50 km (1.7 GPa) beneath Southern Tibet (Sheehan et al., 2014) are less likely to be due to the position of the present-day transition. They could, however, be the signature in these now lowermost continental units of the irreversible damages caused by transition at lower pressure during burial. The use of this reflector as a present-day crustal geothermometer might therefore be less relevant at higher pressures.

6 Acknowledgement

This project was funded by the European Research Council grant REALISM (2016-grant 681346) led by A. Schubnel. We thank prof. Ross Angel for particularly constructive comments and discussions at the early stage of this study.

References

Abers, G. A., & Hacker, B. R. (2016). A matlab toolbox and e xcel workbook for calculating the densities, seismic wave speeds, and major element composition of minerals and rocks at pressure and temperature. *Geochemistry, Geophysics, Geosystems*, *17*(2), 616–624.

Angel, R. J., Alvaro, M., Miletich, R., & Nestola, F. (2017). A simple and generalised p–t–v eos for continuous phase transitions, implemented in eosfit and applied to quartz. *Contributions to Mineralogy and Petrology*, *172*(5), 29.

Bachmann, F., Hielscher, R., & Schaeben, H. (2010). Texture analysis with mtex–free and open-source software toolbox. In *Solid state phenomena* (Vol. 160, pp. 63–68).

Bagdassarov, N., & Delépine, N. (2004). α–β inversion in quartz from low frequency electrical impedance spectroscopy. *Journal of Physics and Chemistry of Solids*, *65*(8-9), 1517–1526.

Berman, R. G. (1988). Internally-consistent thermodynamic data for minerals in the system na2o-k2o-cao-mgo-feo-fe2o3-al2o3-sio2-tio2-h2o-co2. *Journal of petrology*, *29*(2), 445–522.

Birch, F. (1960). The velocity of compressional waves in rocks to 10 kilobars: 1. *Journal of Geophysical Research*, *65*(4), 1083–1102.

Birch, F. (1961). The velocity of compressional waves in rocks to 10 kilobars: 2. *Journal of Geophysical Research*, *66*(7), 2199–2224.

Carpenter, M. A., Salje, E. K., Graeme-Barber, A., Wruck, B., Dove, M. T., & Knight, K. S. (1998). Calibration of excess thermodynamic properties and elastic constant variations associated with the alpha¡–¿ beta phase transition in quartz. *American mineralogist*, *83*(1-2), 2–22.

Cohen, L. H., & Klement Jr, W. (1967). High-low quartz inversion: Determination to 35 kilobars. *Journal of Geophysical Research*, *72*(16), 4245–4251.

Darot, M., Gueguen, Y., Benchemam, Z., & Gaboriaud, R. (1985). Ductile-brittle transition investigated by micro-indentation: results for quartz and olivine. *Physics of the Earth and Planetary Interiors*, *40*(3), 180–186.

Doncieux, A., Stagnol, D., Huger, M., Chotard, T., Gault, C., Ota, T., & Hashimoto, S. (2008). Thermo-elastic behaviour of a natural quartzite: itacolumite. *Journal of materials science*, *43*(12), 4167–4174.

Dorogokupets, P. I. (1995). Equation of state for lambda transition in quartz. *Journal of Geophysical Research: Solid Earth*, *100*(B5), 8489–8499.

Gasc, J., Daigre, C., Moarefvand, A., Deldicque, D., Fauconnier, J., Gardonio, B., … Schubnel, A. (2022). Deep-focus earthquakes: From high-temperature experiments to cold slabs. *Geology*, *50*(9), 1018–1022.

Gibert, B., & Mainprice, D. (2009). Effect of crystal preferred orientations on the thermal diffusivity of quartz polycrystalline aggregates at high temperature. *Tectonophysics*, *465*(1-4), 150–163.

Glover, P., Baud, P., Darot, M., Meredith, P., Boon, S., LeRavalec, M., … Reuschlé, T. (1995). α/β phase transition in quartz monitored using acoustic emissions. *Geophysical Journal International*, *120*(3), 775–782.

Heaney, P. J., & Veblen, D. R. (1991). Observations of the α-β phase transition in quartz: a review of imaging and diffraction studies and some new results. *American mineralogist*, *76*(5-6), 1018–1032.

Holland, T., & Powell, R. (1998). An internally consistent thermodynamic data set for phases of petrological interest. *Journal of metamorphic Geology*, *16*(3), 309–343.

Holyoke III, C. W., & Kronenberg, A. K. (2010). Accurate differential stress measurement using the molten salt cell and solid salt assemblies in the griggs apparatus with applications to strength, piezometers and rheology. *Tectonophysics*, *494*(1-2), 17–31.

Johnson, S. E., Song, W. J., Cook, A. C., Vel, S. S., & Gerbi, C. C. (2021). The quartz α β phase transition: Does it drive damage and reaction in continental crust? *Earth and Planetary Science Letters*, *553*, 116622.

Kern, H. (1978). The effect of high temperature and high confining pressure on compressional wave velocities in quartz-bearing and quartz-free igneous and metamorphic rocks. *Tectonophysics*, *44* (1-4), 185–203.

Kern, H. (1979). Effect of high-low quartz transition on compressional and shear wave velocities in rocks under high pressure. *Physics and Chemistry of Minerals*, *4* (2), 161–171.

Kuo-Chen, H., Wu, F., Jenkins, D., Mechie, J., Roecker, S., Wang, C.-Y., & Huang, B.-S. (2012). Seismic evidence for the α-β quartz transition beneath taiwan from vp/vs tomography. *Geophysical Research Letters*, *39* (22).

Le Chatelier, H. (1890). Sur la dilatation du quartz. *Bulletin de Minéralogie*, *13* (3), 112–118.

Lider, M., & Yurtseven, H. (2014). α-β transition in quartz: Temperature and pressure dependence of the thermodynamic quantities for β-quartz and β-cristobalite as piezoelectric materials. *3D Research*, *5* (4), 1–9.

Mainprice, D., & Casey, M. (1990). The calculated seismic properties of quartz mylonites with typical fabrics: relationship to kinematics and temperature. *Geophysical Journal International*, *103* (3), 599–608.

Marini, L., & Manzella, A. (2005). Possible seismic signature of the α–β quartz transition in the lithosphere of southern tuscany (italy). *Journal of volcanology and geothermal research*, *148* (1-2), 81–97.

McGinn, C., Miranda, E. A., & Hufford, L. J. (2020). The effects of quartz dauphiné twinning on strain localization in a mid-crustal shear zone. *Journal of Structural Geology*, *134*, 103980. Retrieved from `https://www.sciencedirect.com/science/article/pii/S0191814118304851` doi: https://doi.org/10.1016/j.jsg.2020.103980

McKnight, R. E., Moxon, T., Buckley, A., Taylor, P., Darling, T., & Carpenter, M. (2008). Grain size dependence of elastic anomalies accompanying the α–β phase transition in polycrystalline quartz. *Journal of Physics: Condensed Matter*, *20* (7), 075229.

Mechie, J., Sobolev, S. V., Ratschbacher, L., Babeyko, A. Y., Bock, G., Jones, A., ... Zhao, W. (2004). Precise temperature estimation in the tibetan crust from seismic detection of the α-β quartz transition. *Geology*, *32* (7), 601–604.

Meredith, P. G., Knight, K. S., Boon, S. A., & Wood, I. G. (2001). The microscopic origin of thermal cracking in rocks: An investigation by simultaneous time-of-flight neutron diffraction and acoustic emission monitoring. *Geophysical research letters*, *28* (10), 2105–2108.

Minor, A., Rybacki, E., Sintubin, M., Vogel, S., & Wenk, H.-R. (2018). Tracking mechanical dauphiné twin evolution with applied stress in axial compression experiments on a low-grade metamorphic quartzite. *Journal of Structural Geology*, *112*, 81-94. Retrieved from `https://www.sciencedirect.com/science/article/pii/S0191814118301937` doi: https://doi.org/10.1016/j.jsg.2018.04.002

Mirwald, P. W., & Massonne, H.-J. (1980). The low-high quartz and quartz-coesite transition to 40 kbar between 600° and 1600° c and some reconnaissance data on the effect of naalo2 component on the low quartz-coesite transition. *Journal of Geophysical Research: Solid Earth*, *85* (B12), 6983–6990.

Moarefvand, A., Gasc, J., Fauconnier, J., Baïsset, M., Burdette, E., Labrousse, L., & Schubnel, A. (2021). A new generation griggs apparatus with active acoustic monitoring. *Tectonophysics*, 229032.

Nikitin, A., Vasin, R., Balagurov, A., Sobolev, G., & Ponomarev, A. (2006). Investigation of thermal and deformation properties of quartzite in a temperature range of polymorphous α-β transition by neutron diffraction and acoustic emission methods. *Physics of Particles and Nuclei Letters*, *3* (1), 46–53.

Ohno, I. (1995). Temperature variation of elastic properties of α-quartz up to the α-β transition. *Journal of Physics of the Earth*, *43* (2), 157–169.

Ohno, I., Harada, K., & Yoshitomi, C. (2006). Temperature variation of elastic constants of quartz across the α-β transition. *Physics and Chemistry of Minerals*, *33* (1), 1–9.

Schmidt-Mumm, A. (1991). Low frequency acoustic emission from quartz upon heating

from 90 to 610 c. *Physics and Chemistry of Minerals*, *17*(6), 545–553.
Sheehan, A. F., de la Torre, T. L., Monsalve, G., Abers, G. A., & Hacker, B. R. (2014). Physical state of himalayan crust and uppermost mantle: Constraints from seismic attenuation and velocity tomography. *Journal of Geophysical Research: Solid Earth*, *119*(1), 567–580.
Shen, A., Bassett, W., & Chou, I.-M. (1993). The α-β quartz transition at high temperatures and pressures in a diamond-anvil cell by laser interferometry. *American Mineralogist*, *78*(7-8), 694–698.
Van Groos, A. K., & Heege, J. T. (1973). The high-low quartz transition up to 10 kilobars pressure. *The Journal of Geology*, *81*(6), 717–724.
Wenk, H.-R., Barton, N., Bortolotti, M., Vogel, S., Voltolini, M., Lloyd, G., & Gonzalez, G. (2009). Dauphiné twinning and texture memory in polycrystalline quartz. part 3: texture memory during phase transformation. *Physics and Chemistry of Minerals*, *36*(10), 567–583.
Wenk, H.-R., Rybacki, E., Dresen, G., Lonardelli, I., Barton, N., Franz, H., & Gonzalez, G. (2006). Dauphiné twinning and texture memory in polycrystalline quartz. part 1: experimental deformation of novaculite. *Physics and Chemistry of Minerals*, *33*, 667–676.
Zappone, A. S., & Benson, P. M. (2013). Effect of phase transitions on seismic properties of metapelites: A new high-temperature laboratory calibration. *Geology*, *41*(4), 463–466.

Exp. n	Sample	Method	$P_c(GPa)$	$L_0(mm)$	$L_f(mm)$	$T_{\alpha\rightarrow\beta}(^\circ C)$	Duration (min)
$NA_{0.35}$	Novaculite	active	0.35	10.1	9.48	661	46
$NA_{0.5}$	Novaculite	active	0.5	10.5	9.7	720	57
$NA_{0.65}$	Novaculite	”	0.65	10.3	10.2	753	112
$NA_{0.8}$	Novaculite	”	0.8	10.39	9.9	770	150
$NA_{0.9}$	Novaculite	”	0.9	9.3	9	766	78
NA_1	Novaculite	”	1	10.4	10.3	781	107
NA_1^*	Novaculite	”	1	9.6	9.4	–	–
$NA_{1.25}$	Novaculite	”	1.25	10.1	9.9	824	97
$NP_{0.5}$	Novaculite	passive	0.5	10.94	10.1	–	71
$NP_{0.8}$	Novaculite	”	0.8	11	10.3	–	120
$SA_{0.5a}$	S.C a-axis	active	0.5	11	10.8	720	86
$SA_{0.5c}$	S.C c-axis	”	0.5	10.1	10.0	695	53
$SA_{0.8a}$	S.C a-axis	”	0.8	11	10.4	750	100
$SA_{0.8c}$	S.C c-axis	”	0.8	10.9	10.3	742	81

Table 1. Summary of experimental conditions. The transition temperature refers to the conditions where the minimum in P-wave velocity was detected. The experimental duration refers to the time at high pressure during which the temperature was increased. Abbreviations: N for Novaculite, S for Single-crystal, A for active and P for passive acoustic monitoring. $*$ Contrary to NA_1 and all of the other experiments, this one remained in the α-quartz field.

Sample	Number of EBSD maps	Mean grain size (μm)	Mean aspect ratio	Mean shape factor	Mean Twin. Ratio %	Deviation. %
Starting material	1	5.51	1.34	1.44	0.40	—
$NA_{0.5}$	3	4.08	1.47	1.66	19.2	3.3
$NA_{0.65}$	9	4.41	1.53	1.45	6.30	0.7
$NA_{0.8}$	3	3.50	1.42	1.56	19.2	3.4
NA_1	3	4.34	1.47	1.53	18.7	0.3
$NA_{1.25}$	9	4.00	1.63	1.46	8.90	3.6
NA_1^*	2	4.86	1.37	1.46	8.00	0.8

Table 2. Result of EBSD analysis of starting material (Novaculite), sample of experiments on novaculite. Grain size is in μm. Twinning ratio is the total length of Dauphiné twin boundaries over the total length of grain boundaries. The two rightmost columns give the mean value of the twinning ratio its standard deviation. Experiment NA_1^* remained in the α-quartz field and didn't cross the transition.

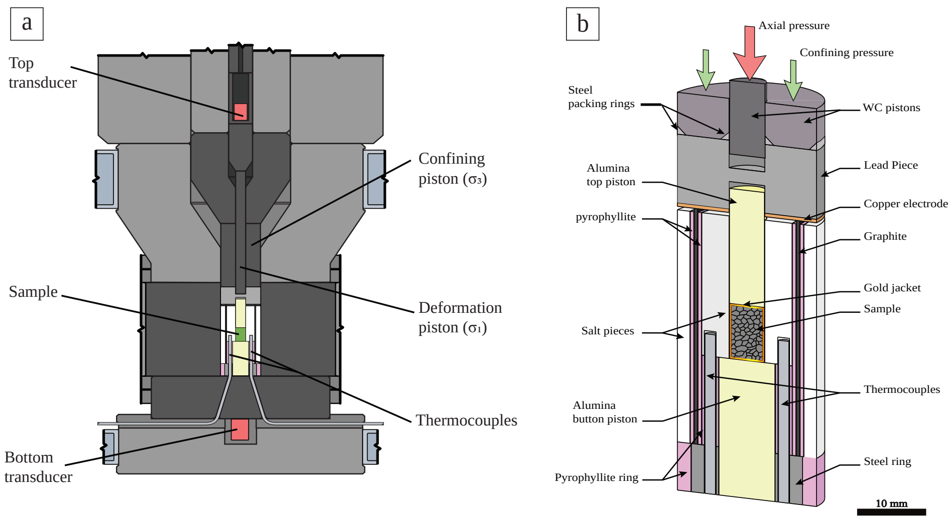

Figure 1. (a) Vertical cross-section of the sample assembly. (b) Schematics of the *Griggs* set-up with the position of the sample assembly and of the ultrasonic transducers.

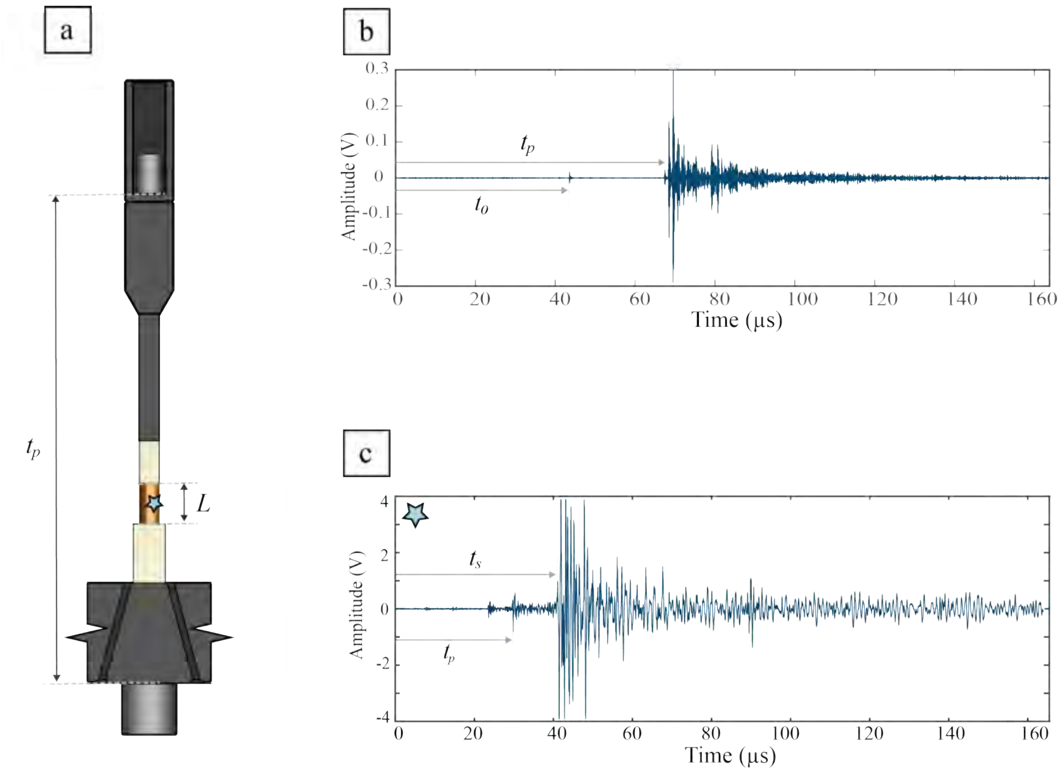

Figure 2. (a) Acoustic monitoring set-up. t_p is the travel time between the two transducers and L the sample length (b) Typical waveform recorded by the top transducer during a velocity survey. t_o is the time at which the pulse is sent to the bottom transducer. (c) Typical waveform of an acoustic emission generated inside the sample and recorded by bottom transducer, amplified at 60 dB and high-pass filtered above 500 KHz.

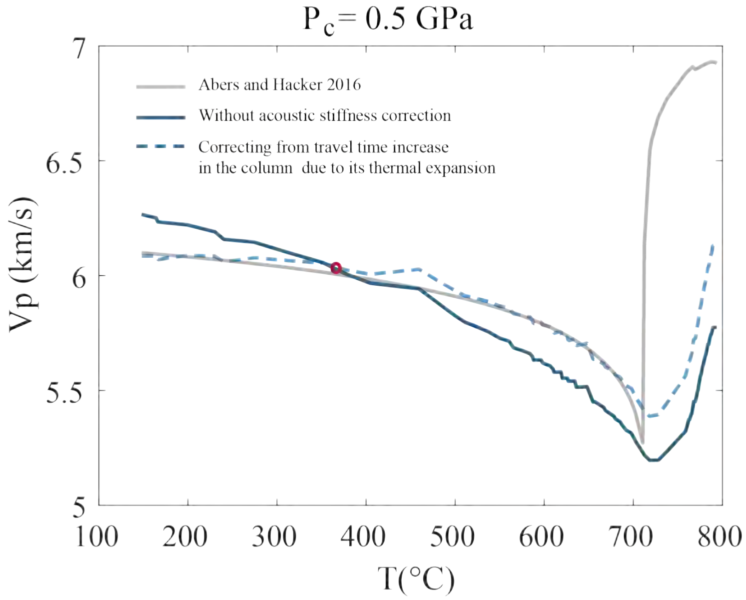

Figure 3. P wave velocity (V_p) versus temperature. The gray solid line represents V_p calculated using (Abers & Hacker, 2016) code at experimental pressure and temperature conditions. The blue solid and dashed lines represent V_p calculated from arrival times, with (dashed line) and without (solid line) correcting the travel-times from the thermal expansion of the loading column. $V_p(0.5GPa, 350^oC)$ (red dot) is our anchor point, which was set to match (Abers & Hacker, 2016)'s prediction.

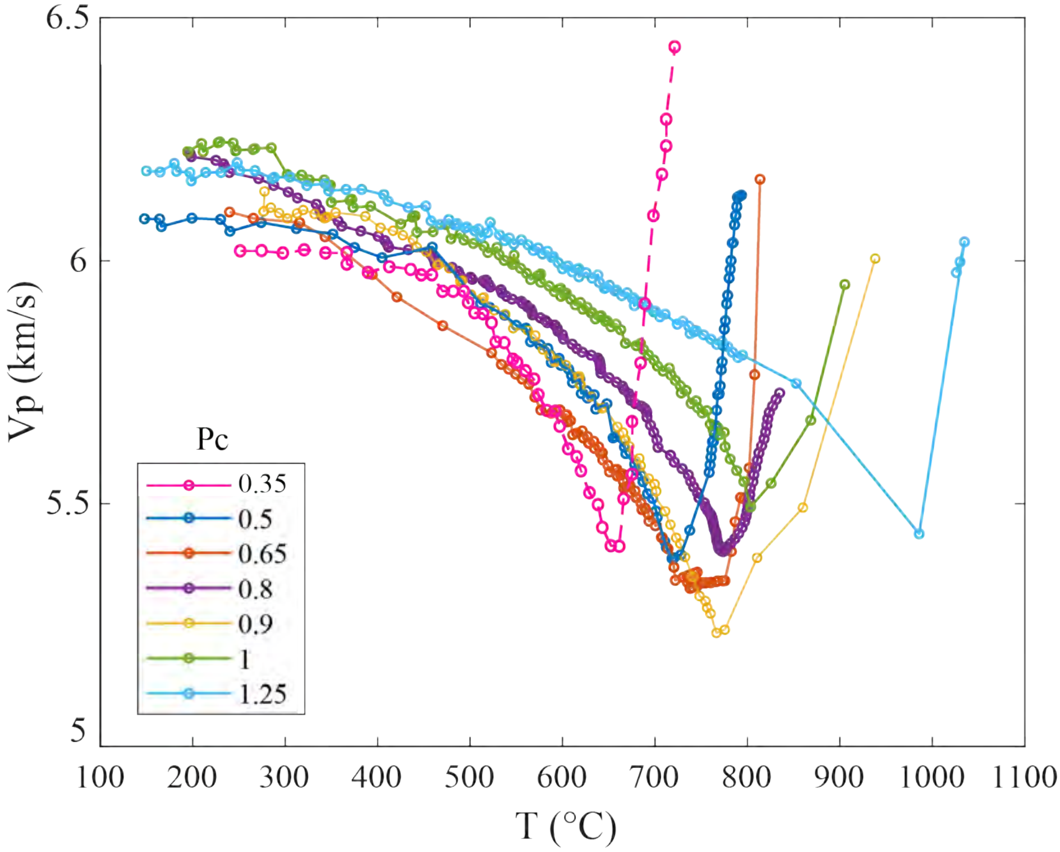

Figure 4. P wave velocity (V_p) versus temperature for confining pressure ranging from 0.35 to 1.25 GPa. Velocities were calculated relative to a reference point at 350°C (gray solid line, see section 2.4 for details).

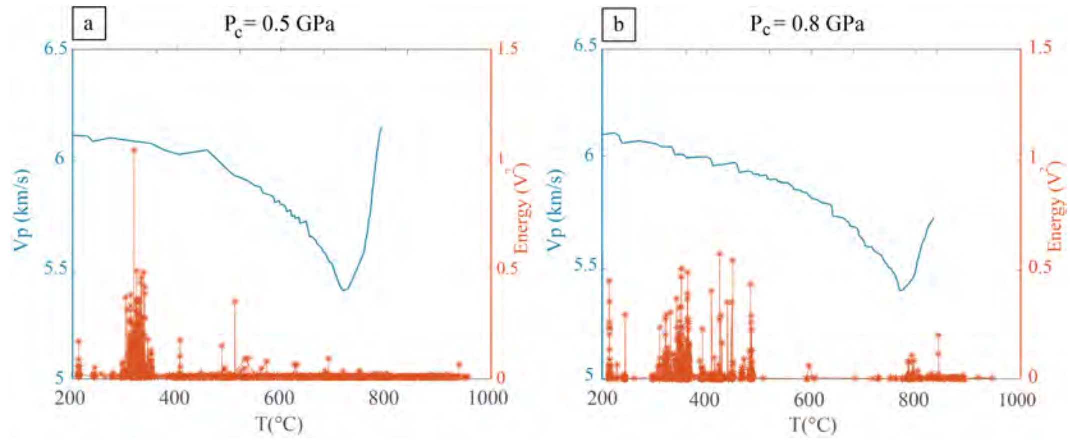

Figure 5. P wave velocity (left blue axis) and acoustic emission energy (right red axis) versus temperature at (a) 0.5 GPa and (b) 0.8 GPa confining pressure. Each star represents an acoustic emission. Note that each subplot also displays two different experiments ($NA_{0.5}$ and $NP_{0.5}$ 0.5 GPa and $NA_{0.8}$ and $NP_{0.8}$ at 0.5 GPa) since our current system does not allow doing both active and passive acoustic monitoring concurrently.

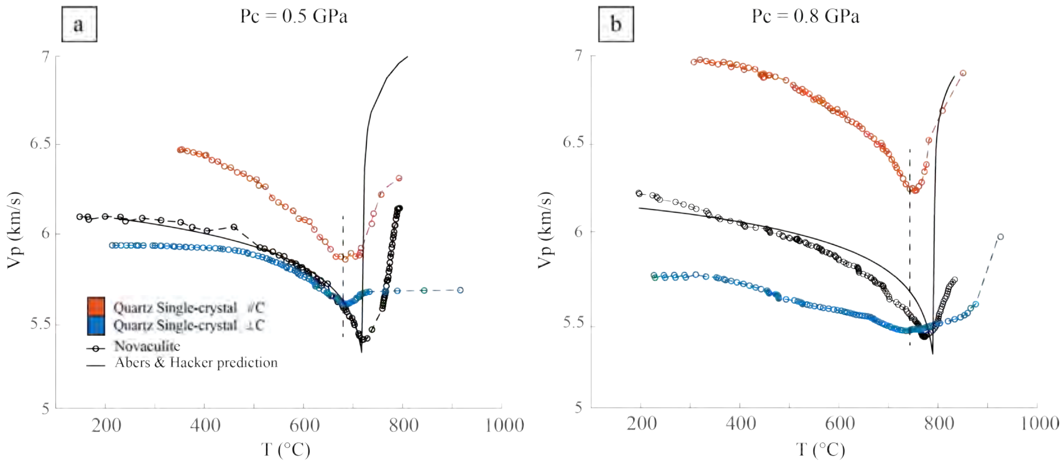

Figure 6. P wave velocities in novaculite versus quartz single crystal. Black solid lines represent the prediction of Abers and Hacker (2016), black circles are the present data obtained on Novaculite, red and blue circles are from single crystal c-axis-parallel and -perpendicular measurements, respectively. (a) 0.5 GPa (experiments $SA_{0.5a}$ and $SA_{0.5c}$) and (b) 0.8 GPa (experiments $SA_{0.8a}$ and $SA_{0.8c}$)

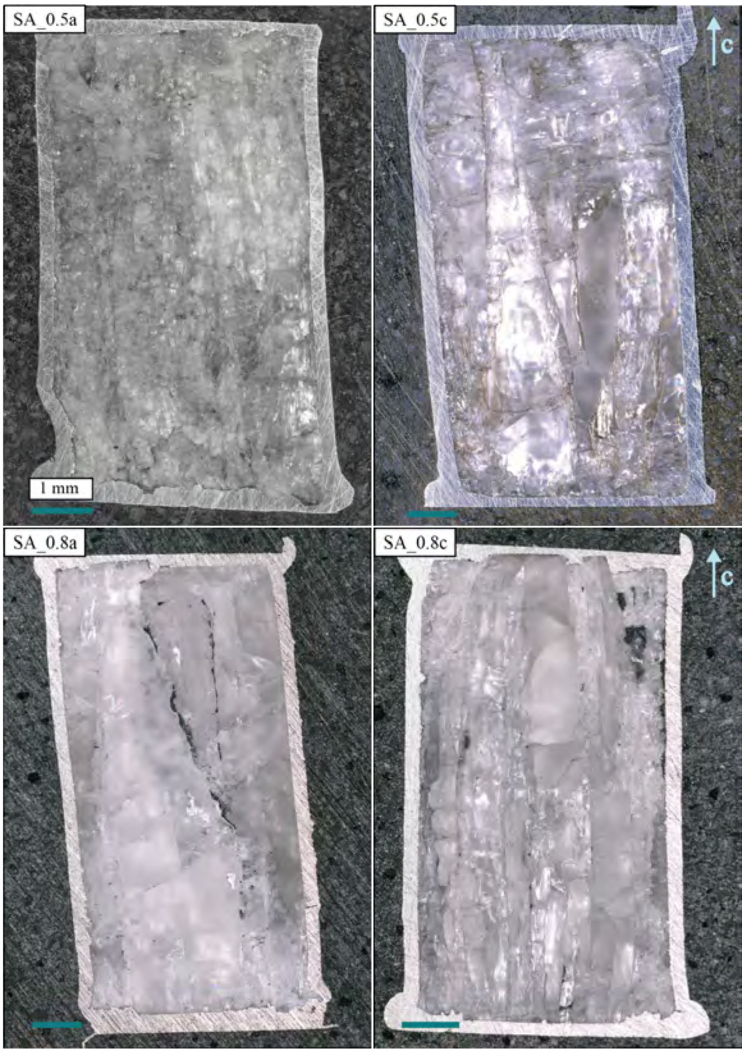

Figure 7. Images of quartz single-crystal samples from experiments at 0.5 and 0.8 GPa. Samples were cored parallel to c-axis and the other two perpendicular to c-axis, as indicated in the top right corner of each image. Scale bar is 1 mm long on all images. The vertical and horizontal cracks are not present in the samples prior to the experiment; their origin is discussed in section 3.3

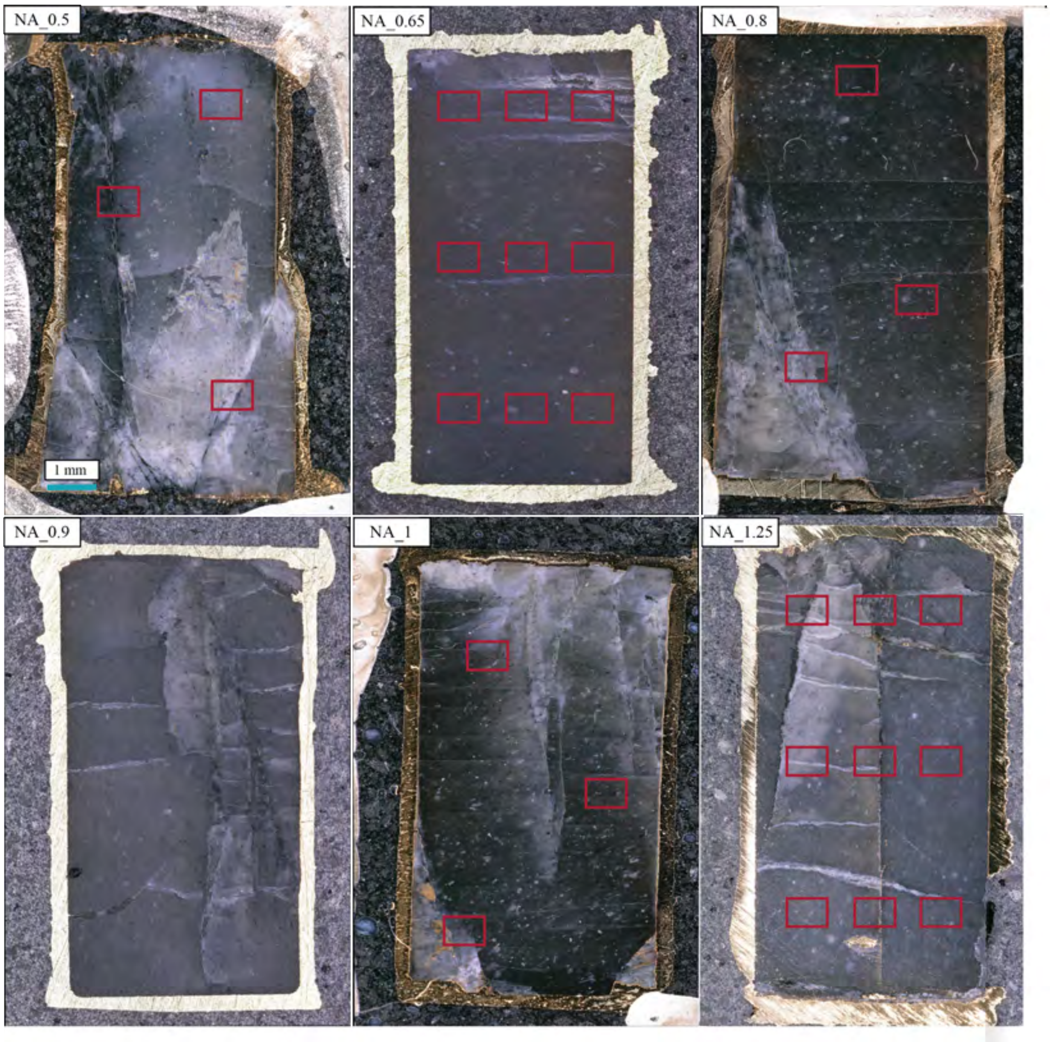

Figure 8. Images of Novaculite samples from experiments at 0.5, 0.65, 0.8, 0.9, 1 and 1.25 GPa. Red rectangles represent zones with EBSD analyses.

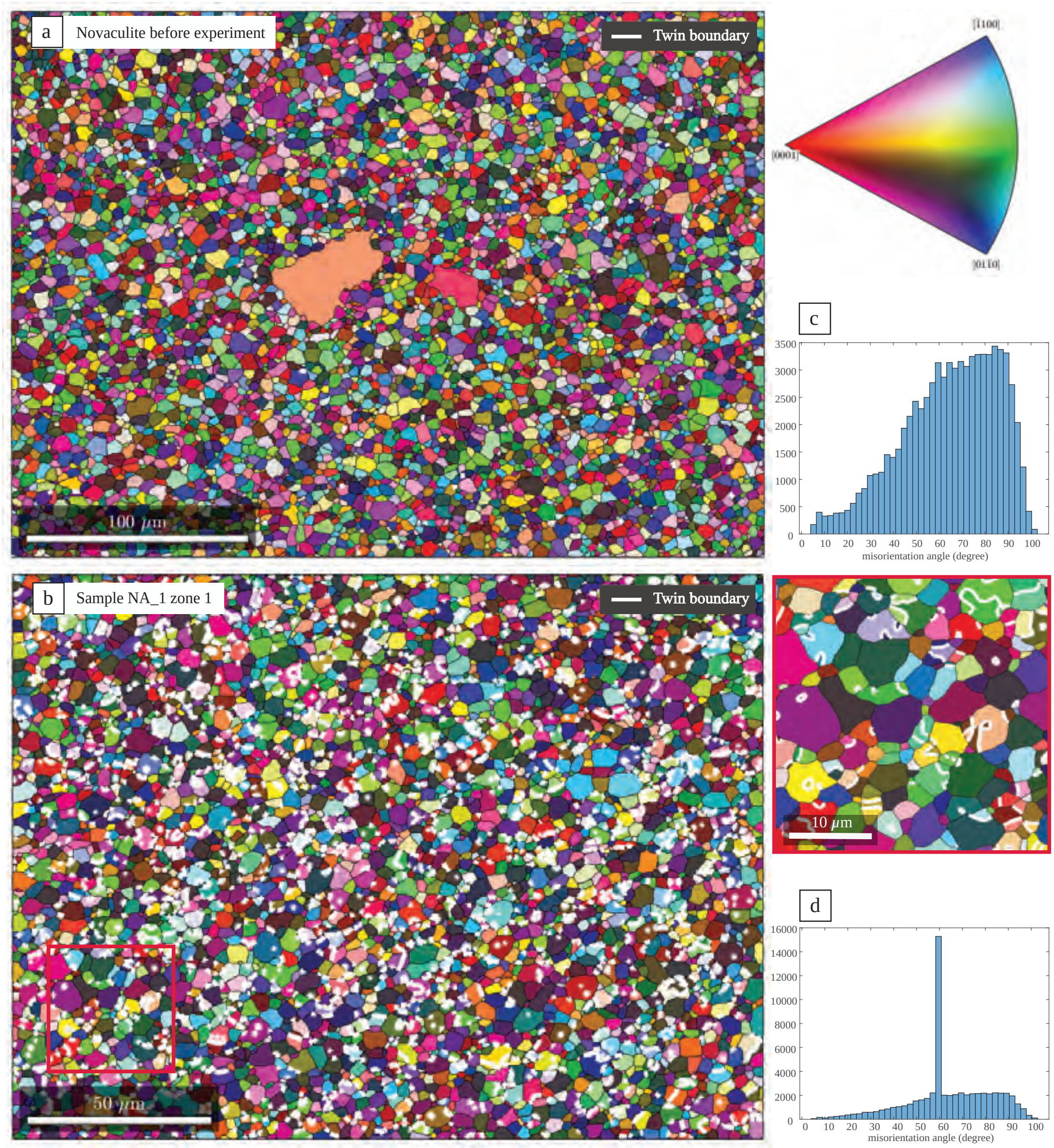

Figure 9. Electron Back Scatter Diffraction (EBSD) image of (a) the novaculite starting material and (b) sample of experiment NA_1 at 1 GPa. White lines represent Dauphiné twin boundaries. (c) and (d) are histograms of novaculite grain misorientations for maps shown in (a) and (b), respectively. The red rectangle on the right shows a magnified view according to the rectangle in (b).

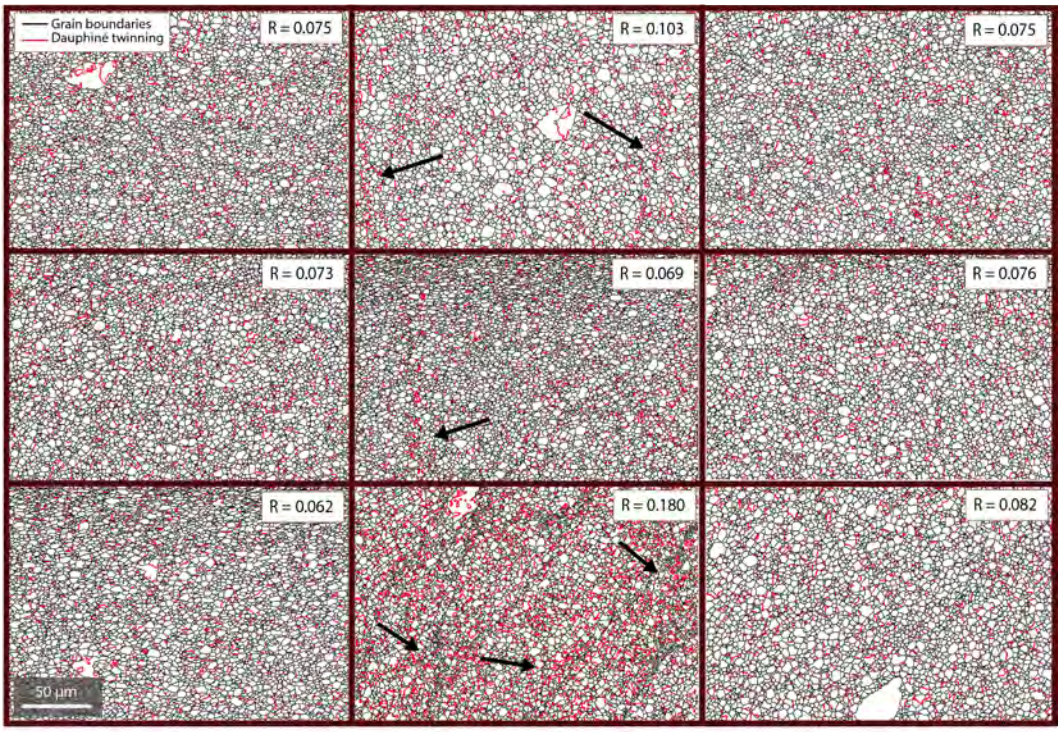

Figure 10. Dauphiné twin boundaries calculated from EBSD images on sample $NA_{1.25}$. R is the twinning ratio. Cracks, which display a higher density of twins are pointed out by arrows.

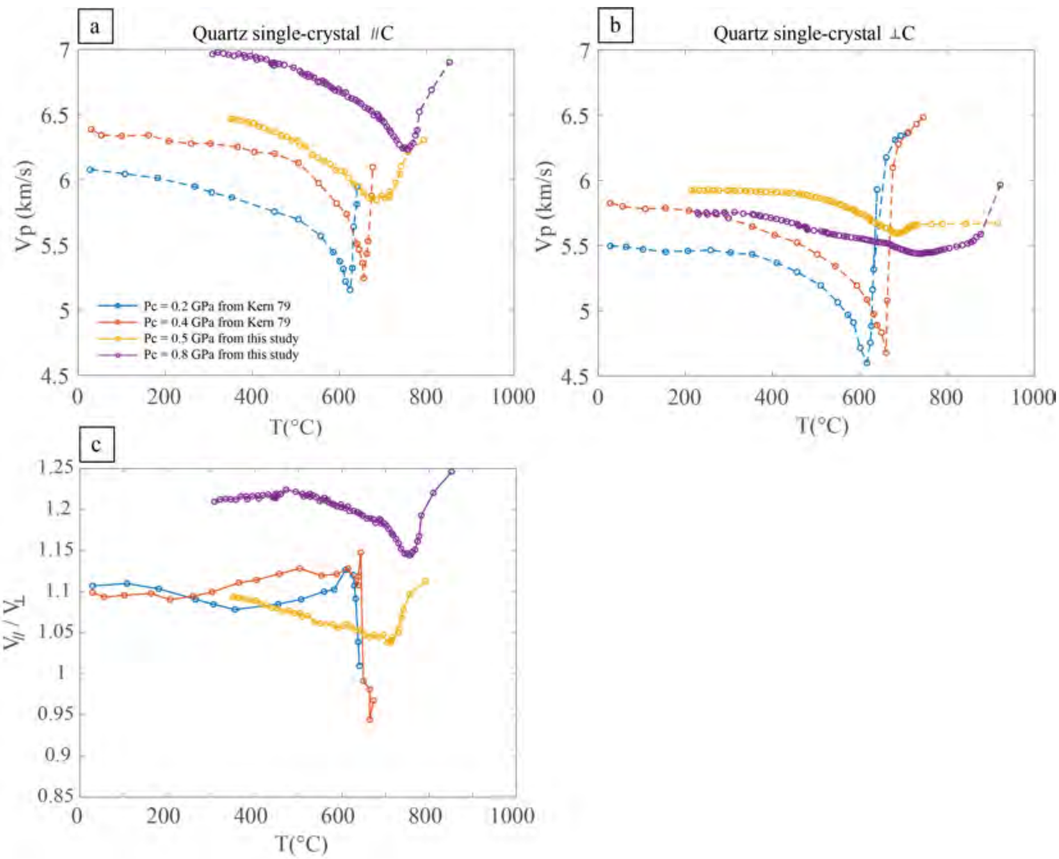

Figure 11. P-wave velocity in quartz single crystals versus temperature (a) $V_{\parallel c}$ along the c-axis, (b) $V_{\perp c}$ along the a-axis, and (c) P-wave anisotropy $V_{\parallel}/V_{\perp}$. The yellow and purple curves represent data obtained at 0.5 and 0.8 GPa, respectively. The blue and red curves represent experimental data from (Kern, 1979) at 0.2 and 0.4 GPa, respectively.

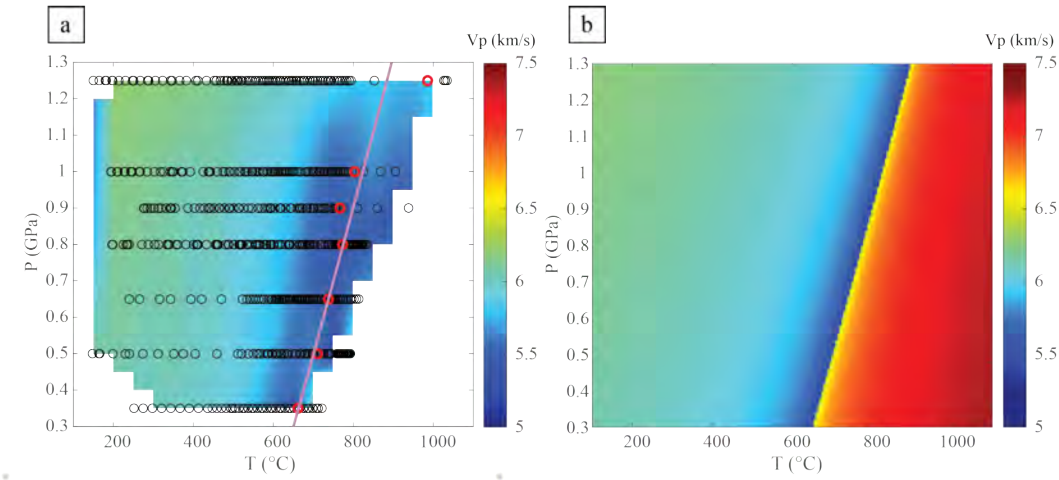

Figure 12. (a) P-wave velocity of quartz as a function of pressure and temperature. P-T conditions for $\alpha \rightarrow \beta$ transition (black solid line) is from (Shen et al., 1993). a) interpolation of experimentally derived P-wave velocities. Black circles correspond to data points; red circles to the P-T conditions at which the minimum P-wave velocity was observed of each experiment, the gray data point represents the reference point (see 2.4). (b) P-wave velocity prediction from (Abers & Hacker, 2016). The colorbar is the same for both panels.

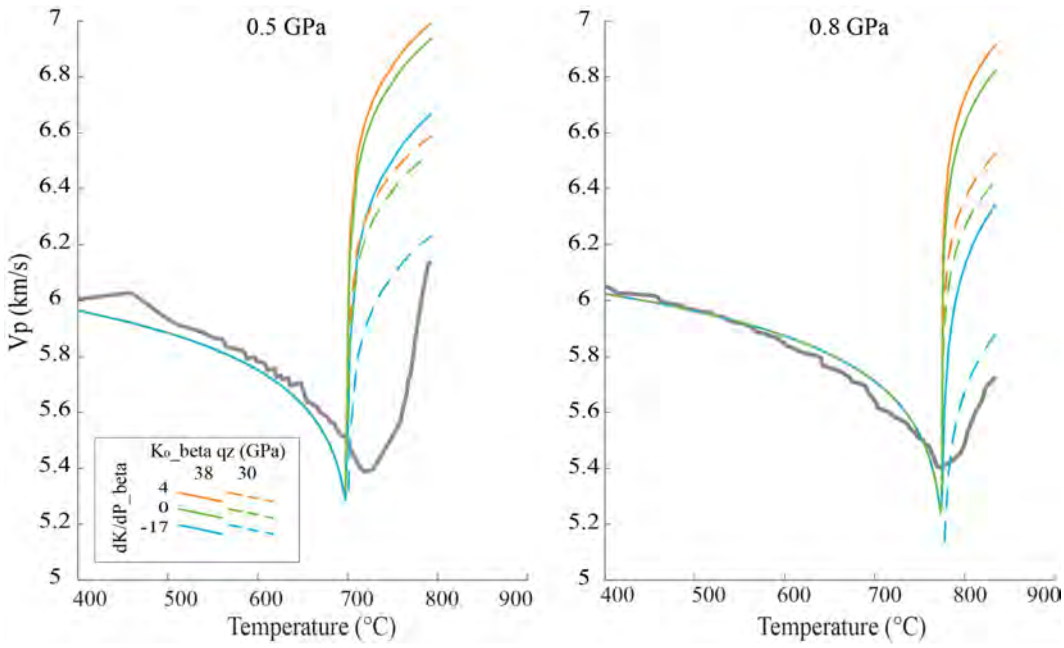

Figure 13. P wave velocity versus temperature at 0.5 GPa (left) and 0.8 GPa (right). Black circles represent our experimental data, black solid line represents the prediction of Abers and Hacker (2016) at experimental pressure and temperature conditions (i.e., with no temperature gradient). Blue, orange and red line are calculated from (Abers & Hacker, 2016) code assuming linear temperature gradients of -50C, -100C and -200C inside the sample.

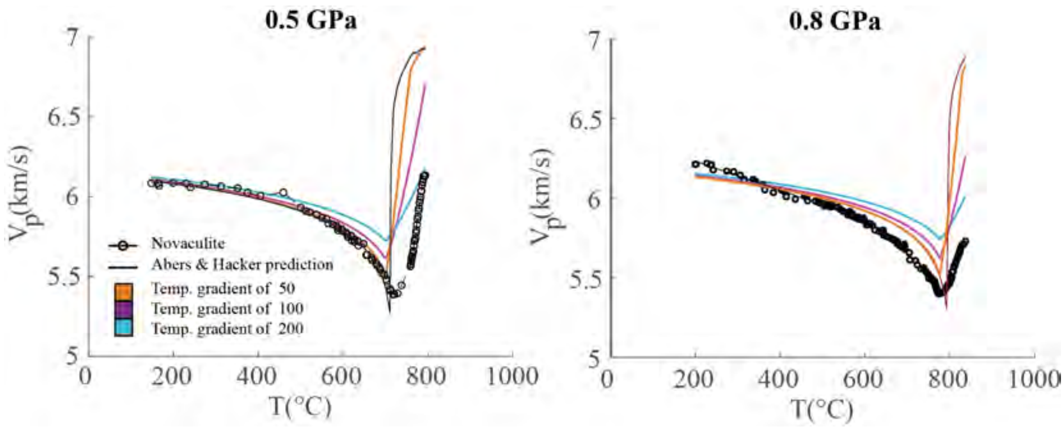

Figure 14. P-wave velocity vs temperature for different values of K_o and $K'(= dK/dP)$ for β quartz. Left, 0.5 GPa; right, 0.8 GPa. Gray solid lines represent data points obtained in this study. Solid and dashed lines are calculations with room pressure bulk moduli of $K_o = 38$ GPa and $K_o = 30$ GPa, respectively. Orange, green and blue curves represent calculations for K' equal to of 4, 0, and -17 respectively.

P-wave velocities across the $\alpha \rightarrow \beta$ quartz transition at lower continental crust pressure and temperature conditions

Arefeh Moarefvand[1] Julien Gasc[1] Damien Deldicque[1] Loic Labrousse[2] Alexandre Schubnel[1]

[1]Laboratoire de Géologie, École Normale Supérieure/CNRS UMR 8538, PSL University, Paris, France
[2]ISTEP, Sorbonne Université, Paris, France

Key Points:

- P-wave velocities measured in quartz at pressure and conditions of the continental lower crust
- $\alpha \rightarrow \beta$ quartz transition was observed as a minimum in P-wave velocities, preceded by important softening
- Our results suggest the velocity change due to the transition decreases with increasing pressure

Corresponding author: Arefeh Moarefvand, `arefeh.maaref@gmail.com`

Abstract

The quartz $\alpha \rightarrow \beta$ transition is a displacive phase transition associated with a significant change in elastic properties. However, the elastic properties of quartz at high-pressure and temperature remain poorly constrained experimentally, particularly within the field of β-quartz. Here, we conducted an experimental study on the quartz $\alpha \rightarrow \beta$ transition during which P-wave velocities were measured in-situ at pressure (from 0.5 to 1.25 GPa) and temperature (200 to 900 °C) conditions of the continental lower crust. Experiments were carried out on samples of microcrystalline material (grain size of 3-6 μm) and single-crystals. In all these, the transition was observed as a minimum in P-wave velocities, preceded by an important softening while P-wave velocities measured in the β-quartz field were systematically lower than that predicted by thermodynamic databases. Additional experiments during which acoustic emission (AE) were monitored showed no significant peak of AEs near or at the transition temperature. Microstructural analysis nevertheless revealed the importance of microcracking while Electron Back-Scatter Diffraction (EBSD) imaging on polycrystalline samples revealed a prevalence of Dauphiné twinning in samples that underwent through the transition. Our results suggest that the velocity change due to the transition known at low pressure might be less important at higher pressure, implying a change in the relative compressibilities of α and β quartz. If true, the velocity changes related to the $\alpha \rightarrow \beta$ quartz transition at lower crustal conditions might be lower than that expected in thickened continental crust.

Plain Language Summary

Phase transitions occurring in minerals at high pressures and temperatures can cause seismological discontinuities, and they happen when the mineral structure transforms from its stable form at lower pressures to a different structure at higher pressures and temperatures. One such transition that has a significant seismic signature is the alpha-beta quartz transition. Seismologists use this signature to determine the temperature conditions in the Earth's crust at depths much greater than those achievable in laboratory experiments. However, the uncertainty arises due to the fact that the alpha-beta quartz transition has only been observed under low-pressure conditions, and it is unclear whether it actually occurs at greater depths. In order to address this, we conducted a series of experiments at increasing confining pressures up to 1.25 GPa (equivalent to a depth of 35 km) and found that the transition becomes less sharp at high pressure. Our results suggest that the transition should not be as sharp as previously thought in seismological images at these depths.

1 Introduction

Trigonal α-quartz transforms to hexagonal β-quartz through a displacive polymorphic phase transformation. At atmospheric pressure, this transition occurs at 575 °C (Le Chatelier, 1890) and the transition temperature increases with pressure. The quartz $\alpha \rightarrow \beta$ transition has been detected in the laboratory up to 3 GPa by different experimental methods (Cohen & Klement Jr, 1967; Mirwald & Massonne, 1980; Van Groos & Heege, 1973; Shen et al., 1993; Bagdassarov & Delépine, 2004) and for single crystals, the Clapeyron slope of the transition is $\sim$ 0.25 K/MPa as reported by (Shen et al., 1993) using laser interferometry.

The $\alpha \rightarrow \beta$ quartz transition is also known for being a λ-transition (Dorogokupets, 1995; Angel et al., 2017), for which the behavior of the first derivatives in volume with respect to P (pressure) and T (temperature) makes it difficult to calculate the pressure and temperature dependence of thermodynamic properties. This arises from the impossibility to extrapolate thermodynamic functions of the low temperature phase (α) into the stability field of the high-temperature phase, and conversely it is impossible to extrapolate functions of the high-temperature phase (β) down to lower temperatures (Dorogokupets, 1995). Nevertheless, parameters used in most thermodynamic databases consist of extrapolations of low pressure experimental data. Berman (1988) introduces a λ-term in the expression of heat capacity C_p, fitted at low pressure for its dependence on T and assumed to be independent of P. Holland and Powell (1998) used the Landau formalism with a dependence in P. Abers and Hacker (2016) use a null thermal expansion coefficient for the β phase and extrapolate the fitting of low pressure K (isothermal bulk modulus) dependence on T at higher pressure, assuming dK/dP to be equal to 4 in the β field, in order to simplify the finite strain estimate used in the density and K calculations. Eventually, Dorogokupets (1995) elaborates a different approach, combining a quadratic T dependence on heat capacity and a derivative of thermal expansion depending on P and using the Murnaghan equation. Overall, all these extrapolations predict a drastic jump in K, and hence in P-wave velocities at the $\alpha \rightarrow \beta$ quartz transition.

Sharp velocity contrasts detected in the seismological record have been attributed to this expected jump at the $\alpha \rightarrow \beta$ quartz transition. In the southern Tuscany geothermal fields, a high amplitude seismic reflection between 3 and 9 km depth has been ascribed to the $\alpha \rightarrow \beta$ transition (Marini & Manzella, 2005; Zappone & Benson, 2013). Using the extrapolation of the transition temperature towards higher pressures, the $\alpha \rightarrow \beta$ quartz transition has also been used in several studies by seismologists to constrain the temperature profile of the lower crust. For instance, a significant increase in V_P/V_S at $\sim$ 50 km depth beneath southern Tibet has been interpreted as a result of the $\alpha \rightarrow \beta$ quartz transition by Sheehan et al. (2014). However, Kuo-Chen et al. (2012) observed V_P/V_S shallower anomalies at $\sim$ 24 km depth beneath Taiwan that they also ascribed to the $\alpha \rightarrow \beta$ quartz transition. Similarly, Mechie et al. (2004) observed a seismic discontinuity at 15 to 20 km deep under Tibet and interpreted it as the $\alpha \rightarrow \beta$ quartz transition.

Besides its seismological signature, the $\alpha \rightarrow \beta$ quartz transition itself has been considered as a potential weakening mechanism for the continental crust, due to the transient drop in elastic strength and the expected large thermal expansion in the vicinity of the transition (Mainprice & Casey, 1990; Johnson et al., 2021). The microcracking damage observed in experimental studies (Doncieux et al., 2008) have been considered as responsible for a drastic porosity change beyond the reaction in the Tuscany geothermal fields (Marini & Manzella, 2005; Zappone & Benson, 2013) and the residual stress left by the transition itself has been estimated as high enough to overcome rock strength and promote seismicity (Nikitin et al., 2006). This transition is therefore expected to have a dramatic effect on quartz-bearing crustal rocks through the whole crustal temperature range, if the properties deduced from low pressure experiments are still valid at higher pressure.

At low pressures, the $\alpha \rightarrow \beta$ transition is accompanied by significant changes in elastic properties (Ohno, 1995; Carpenter et al., 1998; Ohno et al., 2006). In apparent contradiction to Birch's law (Birch, 1960, 1961) which states that elastic wave velocities should evolve linearly with density, the transition is accompanied by an increase in wave velocities in the (lower density - high temperature) β-quartz. Maximum P and S wave velocities for quartz aggregate change from 5.95 to 6.4 km/s and from 4 to 3.9 km/s, respectively (Kern, 1979), while P-wave velocity anisotropy actually decreases from 50% in the α field to 15 % in the β field (Gibert & Mainprice, 2009). However and to the best of our knowledge, the effect of the $\alpha \rightarrow \beta$ quartz transition on the elastic wave velocities in quartz has only been investigated by two distinct laboratory studies under pressure, and only up to 0.4 GPa. Using ultrasonic methods, seismic wave velocities have been measured across the transition by Kern (1979) on quartz single crystals, pure quartzite, granite ($\sim$ 21% Qz) and granulite ($\sim$ 28% Qz) samples at 0.2 and 0.4 GPa confining pressure. Zappone and Benson (2013) measured the P-wave velocity across the transition on a micaschist sample, with 36% of quartz, at 0.2, 0.3 and 0.4 GPa confining pressure. Both studies have reported an important decrease of seismic velocities prior to the transition and a sudden increase - yet generally lower than that predicted by the thermodynamic databases - of P-wave velocities once in the field of β-quartz. Both studies observe minimum in elastic wave-velocities at P-T conditions compatible with the occurrence of the transition. Yet, Kern (1979) also observed an apparent higher transition temperature for granite and granulite, when compared to quartzite and quartz single crystals at the same pressure conditions.

In summary, and despite more than a hundred years of studies, the elastic properties of quartz at high pressure remain poorly known, particularly within the β quartz field. Here, using a new set-up (Moarefvand et al., 2021), we document *in situ* the evolution of P-wave velocities of quartz aggregates and single crystals, duringtemperature crossing of the $\alpha \to \beta$ quartz transition at pressures ranging from 0.35 to 1.25 GPa. Additional experiments were performed using acoustic emission recording as a probe to study the occurrence of microcracking during the transition. Microstructures within our recovered samples were also investigated using Scanning Electron Microscopy (SEM) and Electron Back Scattered Diffraction (EBSD).

2 Materials and Methods

In the following section, we describe the sample preparation and assembly, the experimental set-up and methods, all previously presented by Moarefvand et al. (2021).

2.1 Sample preparation

Our starting material consisted of hard translucent Arkansas novaculite, purchased from a whetstone company based in Arkansas, USA. Novaculite is a dense, hard, fine-grained sedimentary rock, composed of more than 99 percent pure silica. The origin of silica is biogenic, consisting primarily of siliceous skeletal particles of marine organisms such as sponge spicules and radiolaria, and very fine-grained, wind-blown quartz particles. The grains measure between 3 and 6 μm and the initial porosity is below detection threshold. The starting material has been analyzed using EBSD and no crystal preferred orientation has been observed. Four experiments were also performed on a quartz single crystal (of unknown origin), in order to compare the results with those of the microcrystalline novaculite and document the change in V_p anisotropy through the transition at high pressure.

In both cases, cylindrical specimens were cored and manually polished to ensure maximum parallelism of both end-surfaces. Samples were cylinders of 4.5 mm in diameter and 10 mm in length. The exact sample length was measured before each experiment (Table 1). For the single crystal, cores were made either parallel or perpendicular to the c-axis. The sample was then encapsulated in a gold or platinum jacket (0.25 mm wall thickness) and placed at the center of the solid-medium cell assembly (Figure 1.a), where it is surrounded by cold-pressed fine-grained salt pieces, used as confining medium. A graphite furnace, sleeved by two pieces of hard-fired pyrophyllite, is used for heating and two thermocouples measure the temperature inside the assembly. More details on the sample assembly can be found in Moarefvand et al. (2021). After each experiment, the samples was embedded in epoxy and cut along its long axis. Sections were then polished with polishing cloths and diamond paste of decreasing grain size until 0.25 μm and finally, with 0.05 μm colloidal silica, to obtain a highly reflective surface suitable for Electron Back-Scattered Diffraction (EBSD) analysis.

2.2 Experimental set-up

Experiments were performed using the newly installed third-generation Griggs apparatus at the Laboratoire de Géologie of École Normale Supérieure Paris, designed to perform deformation experiments at P-T conditions up to 5 GPa and 1000 °C. This apparatus is a modified piston cylinder apparatus used to generate a controlled environment of high pressure, high temperature and deviatoric stress. At the core of this apparatus lies the 20 mm diameter solid-medium sample assembly (Figure 1.a). Axial load (σ_1) is applied via a series of alumina and tungsten carbide (WC) pistons of 5 mm diameter, above the specimen. The confining pressure (σ_3) is transmitted via a cylindrical WC piston of 20 mm in diameter to the cell assembly (Figure 1.a and b). Confining and differential stresses are driven via two servo-controlled high pressure precision micro-volumetric pumps and during the experiments, a set of three LVDTs (Linear Variable Differential Transducers) allows us to measure the relative displacement of the confining and differential stress pistons. The stiffness of the apparatus was calibrated and found to be 20 μm/kN. Temperature gradients inside the cell assembly were also previously assessed by Moarefvand et al. (2021).

In this study, all experiments were carried out at constant confining pressure, maintaining the conditions as close as possible to hydrostatic (no measurable differential stress). Experiments were performed at pressures ranging from 0.35 to 1.25 GPa. The pressure was first slowly raised under moderate temperature conditions (typically 100-200 °C). Once the target pressure was reached, the temperature was increased at a rate of 10 °C/ min, from 200 to 1000 °C (above the transition temperature), and then quenched. To compensate for thermal pressure during the ramping of temperature, the confining pressure was maintained constant and the differential stress close to zero by enabling both the confining and differential stress pistons to slowly retract, using the servo-controlled pumps in constant pressure mode. The thermal expansion of the axial (σ_1) column was measured this way and found to be 1μm/K. Parameters recorded every second during the experiment include displacements ($\pm$0.1 μm), axial (σ_1) and confining (σ_3) stresses ($\pm$ 0.05 GPa) and temperature ($\pm$ 20 °C). More details on the experimental set-up and calibration procedures can be found in Moarefvand et al. (2021).

2.3 Active and passive acoustic monitoring set-up

Two high-frequency (5-10 MHz) industrial piezoelectric transducers were used for active acoustic monitoring to measure P-wave velocities during the experiment. The bottom transducer (Olympus V110, P-wave, 5 MHz center frequency) is located below the sample assembly, glued directly under the baseplate (Figure 1.b). The bottom transducer, used as the ultrasonic source, is connected to a software-controlled pulse-box custom-made by Eurosonics/Mistras. Electric impulses of 250 V , 0.1 μs long, are sent at 1kHz repetition rate to the bottom transducer, which converts these electric pulses into planar guided P-waves propagating along the deformation column. The top transducer (Olympus V129, P-wave, 10 MHz center frequency) is located above the sample assembly, glued on a tungsten carbide (WC) spacer placed within the deformation column. The top transducer, used as the ultrasonic receiver, is amplified at 38 dB. Note that a 5-10MHz frequency corresponds, for a P-wave velocity of 5 km/s, to 0.5-1 mm wavelength, i.e. 10 to 20 times smaller than the sample's length.

To increase the signal-to-noise ratio, stacks of 1000 waveforms, synchronized by the pulse box, were recorded every minute during the experiment. Stacked waveforms are collected with a sampling frequency of 50 MHz. A typical stacked waveform recorded by the top transducer during an experiment is represented on figure 2.b, where t_o and t_p represent the time of pulsing and the arrival time of the P-wave on the top transducer, respectively, $(t_p - t_o)$ thus representing the travel time between both transducers. The acoustic stiffness, i.e., the travel time delay due to the shortening of the column upon axial loading (3 ns/kN), and temperature dependence (0.4 ns/K) of the travel time through the column were also calibrated, discussed and interpreted by Moarefvand et al. (2021).

To record acoustic emissions, an S-wave transducer (Olympus V156, 5 MHz center frequency) was used instead as bottom transducer (Fig. 2.a). The S-wave transducer being sensitive to both S and P waves, the arrival time difference $(t_p - t_s)$ of both waves can be used as a proxy for 1D localization along the column. AEs are detected using a 60 db amplifications and a simple threshold logic. Whenever the threshold is crossed, waveforms are collected at a 50MHz sampling frequency and the signal is recorded both non-amplified and amplified (at 30 dB and 60 dB). Gasc et al. (2022) have demonstrated that the AE system is sensitive to the propagation of cracks ranging from a few tens of μm to a few mm in size. One example of recorded waveforms is illustrated on figure 2.c.

2.4 Data processing and P-wave velocity measurements

P-wave arrival times and time-differences are determined using a cross correlation (CCR) algorithm in reference to a master waveform, which is manually picked. Prior to the CCR, waveforms are resampled at 100 MHz using a spline interpolation function, so that the resolution of the measured time-differences is of the order of 10 ns. This pre-processing of the acoustic data is performed using the software Insite (Applied Seismology Consulting). The PZT transducers are not directly in contact with the sample (figure 2.a) and most of the travel time actually occurs along the axial column between the two transducers. The travel time through the column, and its pressure and temperature dependencies, therefore need to be precisely calibrated in order to calculate the P-wave velocity V_p in from the travel time knowing the sample's length.

At any given time during the experiment, we have $t(P,T) = t_s(P,T) + t_c(P,T)$, with $t(P,T)$, $t_s(P,T)$ and $t_c(P,T)$ respectively the measured travel time, the travel time in the sample and travel time in the column. To estimate the initial quartz velocities and their theoretical evolution during the experiments, we use the (Abers & Hacker, 2016) MATLAB® toolbox, which calculates elastic moduli and density of crystals at high pressure and temperature using a database of thermodynamic parameters of 60 minerals. Using this toolbox, we calculate the velocity V_o of α quartz at a reference pressure (0.5 GPa) and temperature (350 °C). Knowing the sample length $L(P,T)$ at this reference temperature and pressure during an experiment on novaculite, we calculate the travel time in the sample $t_s(0.5, 350) = L(0.5, 350)/V_o$. We can then calculate the travel time in the column at 0.5 GPa and 350 °C:

$$t_c(0.5, 350) = t(0.5, 350) - t_s(0.5, 350)$$

Changes in column length due to elastic loading and thermal expansion were determined from deformation and heating calibration experiments, from which both the temperature ($\beta = 0.4ns/K$) and pressure ($k_a = 3ns/kN$) dependencies of the travel time in the column were obtained (Moarefvand et al., 2021). Using the above, we may calculate the travel time in the column at any given P-T conditions:

$$t_c(P,T) = t_c(0.5, 350) - \beta(T - 350) - k_a S_o(P_o - P)$$

where S_o is the sample section area $S_o = \pi r^2$, which is fixed as constant and equal to r = 4.5 mm. Finally, we obtain the P-wave velocity within the sample at any (P,T) by correcting for the travel-time in the column:

$$V_p(P,T) = \frac{L(P,T)}{t_s(P,T)} = \frac{L(P,T)}{t(P,T) - t_c(P,T)}$$

Since t_c can be calculated at given P and T, this method allows us to retrieve P-wave velocities during all of our experiments, using a single reference point at 0.5 GPa and 350 °C, the length of the sample and its evolution during the experiment, $L(P,T)$ being determined independently with the use of an LVDT.

The measured V_p at 0.5 GPa confining pressure (blue curve on Figure 3), when corrected for temperature effects on the travel time through the column (yellow curve on Figure 3) compares remarkably well to the Abers and Hacker (2016) prediction at these experimental conditions (solid gray curve on Figure 3).

Note that all three curves intersect at 0.5 GPa and 350 °C due to the calibration procedure described above. In the following, we chose to correct all travel times for temperature effects and use only one anchorage point at 350 °C/0.5 GPa for all curves (red dot on figure 3) including for quartz single-crystals, so that possible pressure effects are not due to or hidden by calibration artefacts. The actual error bar on these measurements is hard to assess, but we expect an error of $< 10\%$ on corrected velocities, due to small changes in column length between experiments, and a resolution of $\sim 0.1 km/s$ between relative measurements performed within a single experiment.

3 Experimental results

A total of 14 experiments (Table 1) were performed at high pressure and temperature. Experimental conditions and results are summarized in Table 1. Initial and final length of the samples were measured systematically, and in most cases, final shortening was maintained $< 5\%$.

3.1 P-wave velocities evolution during $\alpha \rightarrow \beta$ quartz transition in novaculite at high-pressure

The evolution of P-wave velocities measured on novaculite samples versus temperature are displayed on Figure 4. For all experiments, the P-wave velocity decreases gradually with the temperature and reaches a minimum value, beyond which an abrupt rise is observed. The temperature corresponding to the minimum in velocity is interpreted as being the $\alpha \rightarrow \beta$ quartz transition temperature. As expected, this minimum value in velocity progressively shifts to higher temperatures with increasing confining pressure. Whatever the pressure, the gradual velocity decrease observed in the α-quartz field prior to the transition is almost fully recovered once at high temperature in the β-quartz field. A trend of increasing velocity with increasing pressure is observed in the α-field. At low pressure (0.35 and 0.5 GPa), the maximum values of V_p measured in the β-field are, as expected, higher than those measured at low temperature in α-quartz. However, during the highest pressure experiments, our measures of P-wave velocities within the β-field were limited by the melting point temperature of the confining medium (halite). Once reached, molten salt started to convect, which, changing the radial temperature gradients within the assembly, induced an uncontrolled increase of the temperature in the sample.

Two additional experiments were carried out at 0.5 and 0.8 GPa confining pressure on novaculite using the AE recording set-up, in order to study the mechanical effect of the $\alpha \rightarrow \beta$ transition. Figure 5 compares AE recording experiments with experiments conducted at the same P-T conditions, during which P-wave velocities were measured (nb: unfortunately, our current system does not allow doing both concurrently). Below 400 °C, dozens of AEs were detected upon heating. Note that this low temperature burst of AEs is not accompanied by a sharp decrease in velocities, in such a way that the cracks at the source of the AEs do not seem to affect much the elastic properties of the sample. On the contrary, above 400 °C, while the P-wave velocity softening is strongest, hardly any AEs were detected. At 0.5 GPa, the transition itself is not associated with a detectable burst of AEs. At 0.8 GPa, a burst of AEs was detected close to the transition. Note that this burst is smaller than what was detected at temperatures below 400 °C. From this, we may conclude that there is no significant dynamic microcracking effect during the quartz $\alpha \rightarrow \beta$ transition at high-pressure under hydrostatic stress. However, one should keep in mind that if microcrack propagation is slow (or quasi-static), it can remain unnoticed because of the inherent limitations in the AE detection capability of our system.

3.2 P-wave velocities evolution during the $\alpha \rightarrow \beta$ quartz transition in quartz single-crystals at high-pressure

In order to isolate the possible effect of grain boundaries and intergrain interactions from intra-crysatlline processes on the transition and the evolution of seismic anisotropy through the latter, four additional experiments were carried out on quartz single-crystals. Two samples were cored parallel to the c-axis, and two normal to the c-axis. Experimental conditions and transition temperatures $T_{\alpha \rightarrow \beta}$ are given in Table 1. The evolution of P-wave velocity during these experiments at 0.5 and 0.8 GPa are presented in Figure 6. The P-wave anisotropy of quartz is larger at higher pressure, from a value of $(V_c - V_a)$ of 0.55 km/s at 0.5 GPa and 350 °C to 1.2 km/s at 0.8 GPa and 350 °C. The evolution of P-wave velocities measured in novaculite at the same pressures lies between the ones measured along the slow and fast directions in single crystals, consistently with the random orientation of quartz crystals in novaculite.

The softening prior to the transition, and the subsequent recovery at high temperature, is larger for waves propagating along the c-axis. The P-wave velocities measured in novaculite in the α-quartz field at 0.5 GPa are well-matched by the Abers and Hacker (2016) prediction. The match between the theoretical prediction and our data is not as good at 0.8 GPa, although the amount by which V_p decreases until the transition temperature in our data is also remarkably similar to what is predicted by Abers and Hacker's database. Finally, note that the minimum in P-wave velocity is reached at lower temperatures for single-crystals than for the microcrystalline aggregate at the same pressure (Table 1 and Fig. 6). This difference, also observed by Kern (1979), could either be due to the anisotropy of thermal expansion and compressibility of quartz and/or the pervasive opening of grain boundaries in the microcrystalline aggregates delaying the apparent rise of velocity beyond the transition temperature in novaculite experiments.

3.3 Microstructural analysis

Samples were first imaged in reflected optical light using a digital microscope with a magnification of 200x (Figures 7 and 8). Images of single-crystal samples (Figure 7) demonstrate our samples did not undergo significant shortening (or deformation) as no shear cracks with visible offset can be observed at the sample scale, thus demonstrating the samples underwent the transition in conditions relatively close to hydrostatic. Yet, horizontal and vertical cracks are pervasive and dissect the initial crystals. Microcracking seems to have been more intense at lower pressure (0.5 GPa) and parallel to the c-axis, which may be due to the anisotropic thermal expansion of quartz. Nevertheless, it is impossible to conclude whether the propagation of these microcracks took place at high pressure and temperature conditions, or rather, upon quenching and decompression.

Images of novaculite samples (Figure 8) show no significant shortening, except in $NA_{0.5}$ and $NA_{0.8}$ where shear fractures accompanied by tangential displacement are visible in the lower part of images. Associated shortening is lower than $\sim 7\%$. Yet, fractures without tangential displacement are visible in all samples. Horizontal fractures are interpreted as decompression cracks. The set of vertical cracks, observed in all samples except $NA_{0.65}$ is more intriguing. No apparent displacement is associated to them (mode I). They may have been produced at high pressure and temperature conditions, but they are absent in $NA_{0.65}$) and confining pressure seems to have little effect on their propagation. In any case, quenching and pressure unloading of the sample causes significant transient deviatoric stress, likely responsible for these brittle features, as suggested by the numerous acoustic emissions (AE) recorded in this final step of the experiments.

To complement our microstructural analysis, EBSD maps were acquired on several zones on selected samples, with a step size of 0.5 μm (Figure 9 and Table 2). EBSD maps were then analyzed using the MTEX matlab toolbox (Bachmann et al., 2010), which allows determining grain-boundaries, grain size and shape parameters. Grain boundaries were identified using a misorientation threshold of 13° between neighboring pixels. The results of EBSD analysis of the starting novaculite and our HP-HT samples is summarized in Table 2. In addition, we also analyzed a sample that did not cross the transition, yet underwent 1 GPa of pressure and moderate temperature (700 °C) (NA_1^*). The average grain-size of the starting novaculite is 5.51 μm. Samples that experienced HP-HT conditions present a slight grain-size reduction, with a final grain-size ranging between 3.39 and 4.43 μm, and a slight increase in the grain aspect ratio (Table 2).

We also searched for evidence of Dauphiné twinning, which result in a 60° rotation of the a-axis around the c-axis. Previous studies have shown that the structure of $\beta-$quartz can be described geometrically as a spatial average of two Dauphiné twin configurations (Heaney & Veblen, 1991) and Dauphiné twinning have thus been used as a marker of former $\alpha \rightarrow \beta$ transition in rocks that underwent the $\alpha \rightarrow \beta$ transition (Wenk et al., 2009). Here, we used the ratio between the cumulative twin boundary length to total grain boundary length as a proxy for the amount of Dauphiné twinning. The starting material has a ratio of 0.48%, while samples that underwent the $\alpha \rightarrow \beta$ transition have ratios ranging between 6.3 and 19%. Dauphiné twinning is therefore not inherited from starting material and developed during experiments. Sample NA_1^*, which did not undergo the transition, exhibits a mean twinning ratio of 8% (see Table 2), implying that some Dauphiné twinning also occurred in the α-field. Three of the experiments show a twinning ratio significantly larger or equal to the ratio observed in sample NA_1^*, while the other two show similar values. Sample $NA_{1.25}$ has been extensively mapped to detect any internal heterogeneity in the twinning ratio pattern. Ratio remains fairly uniform throughout sample, except for a small region in the bottom center part, where higher temperatures may have contributed to an increase in twinning ratio (Moarefvand et al., 2021). Dauphiné twinning is also concentrated along cracks, possibly due to higher stress concentrations at the grain boundary scale caused by strain incompatibilities.

4 Discussion

4.1 Microstructural evidence of the transition

Because of the displacive nature of the transition, β-quartz cannot be quenched. In consequence, only a few microstructural arguments exist that may evidence that quartz crystals actually underwent the transition. Among these, microcracking and the occurrence of Dauphiné twins are the most prominent (Johnson et al., 2021; Wenk et al., 2009). Quantitative microstructural data on samples that experienced the transition at high-pressure are still lacking. At atmospheric pressure, laboratory studies have reported microcracking associated to the transition using micro-indentation or acoustic emission (AE) techniques (Darot et al., 1985; Schmidt-Mumm, 1991; Glover et al., 1995; Meredith et al., 2001). Doncieux et al. (2008) demonstrated the irreversibility of crack damage, as only a reduced number of AEs were detected when the temperature was lowered across the reversed ($\beta \rightarrow \alpha$) transition. The $\alpha \rightarrow \beta$ quartz transition being a λ-transition, the occurrence of damage could be explained by the important rise of thermal expansion of α-quartz near the transition (Kern, 1979). Another interpretation is the reduction of the Griffith fracture energy criterion to nearly zero at the transition, as observed by Darot et al. (1985). Here, our postmortem analysis also revealed pervasive mode-I microcracking, although it is difficult to infer whether this microcracking took place at high pressure and temperature conditions or not. In that sense, AE monitoring did reveal that if microcracking took place at high pressure and temperature, it propagated in a quasi-static manner (absence of major AE bursts at or around the transition temperature).

Dauphiné twinning density in experimental products having crossed the $\alpha \rightarrow \beta$ transition is significantly higher than in the reference sample that remained in the α-field. Two experiments, $NA_{1.25}$ and $NA_{0.65}$, showing a P-wave velocity curve symptomatic of the $\alpha \rightarrow \beta$ transition, nevertheless exhibit a low Dauphiné twinning density. The transition therefore does not systematically leave Dauphiné twins behind. Experiment $NA_{0.65}$ is the one with the shortest residence time in the β-field, and experiment $NA_{1.25}$ is the one with the smallest difference between maximum temperature reached and transition temperature (Figure 4). These specificities might explain their lower twin densities. In addition, Dauphiné twins can also result from deviatoric stress (Minor et al., 2018; McGinn et al., 2020). The significance of the Dauphiné twins thus remains a question. Dauphiné twins could either constitute a remnant of the incomplete transformation of α quartz into β, which was imaged under TEM as the growth of Dauphiné twin domains (Heaney & Veblen, 1991) or twins could also emerge as a response to deviatoric stresses caused by strain incompatibilities during the transformation. The differential stress threshold for Dauphiné twinning in quartz aggregates is approximately 50 MPa, which falls well within the uncertainty range of the stresses applied within ab the Griggs apparatus (Moarefvand et al., 2021; Holyoke III & Kronenberg, 2010; Wenk et al., 2006). Unsought deviatoric stress might have developed in some experiments and caused some of the twinning observed. Our sample NA_1^* that did not cross the transition shows a twin density comparable to that of two samples that did ($NA_{0.65}$ and $NA_{1.25}$). These two later experiments show evidences for very low deviatoric stresses, with a very well-preserved sample shape (Figure 8). It is therefore possible that these two experiments, did not develop internal stresses high enough to activate Dauphiné twinning or preserve twins during cooling. These observations, as well as the higher twin density near the most deformed parts of the samples, nevertheless suggest that both the $\alpha \rightarrow \beta$ transition and deviatoric stress can induce the appearance of significant Dauphiné twins (figure 10). The highest twin densities measured here are likely caused by a combination of both mechanisms.

4.2 Comparison with previous experimental data and thermodynamic databases

Our experimental P-wave velocity measurements on quartz single crystals can be compared with those of Kern (1979), performed at 0.2 and 0.4 GPa (Figure 11). In quartz single-crystals, P-wave velocities are faster along the c-axis ($V_{\parallel c}$) at all pressure conditions, in agreement with Kern (1979). $V_{\parallel c}$ also show a positive pressure dependence of $\sim 1.2km/s/GPa$ within the 0.2-0.8 GPa range. However, and in contradiction with the observations of Kern (1979), we observe a negative pressure dependence of the P-wave velocities measured along the a-xis ($V_{\perp c}$) between 0.5 and 0.8GPa, which needs to be experimentally confirmed and reproduced. We observe that the temperature softening before the transition, also observed in Novaculite, is much less pronounced for P-wave velocities propagating along the a-axis than along the c-axis. The velocity jump once in the $\beta-$ field is also more pronounced for $V_{\parallel c}$ than for $V_{\perp c}$. These differences result in significant variations in P-wave anisotropy ($V_{\parallel c}/V_{\perp c}$) across the temperature range investigated. We observe that the anisotropy decreases quasi-linearly when approaching the transition temperature, and increases sharply once in the $\beta-$ quartz field. This late increase in anisotropy has not been observed by Kern (1979) due to the scarcity of data points within the $\beta-$ field. It is nevertheless expected from extrapolations of quartz elastic properties at high temperatures (Mainprice & Casey, 1990).

Experimental P-wave measurements can be interpolated on a P-T diagram for comparison with the thermodynamic predictions using Abers and Hacker (2016) database (Figure 12). Except for experiment $NA_{1.25}$ that yields a minimum P-wave velocity 100 °C higher than expected, the P-wave velocity minimum observed experimentally (red circles on Figure 12) lies between 4 and 35 °C away from the $\alpha \rightarrow \beta$ transition pressure and temperature conditions determined by Shen et al. (1993) using laser interferometry. Considering a ± 25 °C uncertainty on our thermocouple measurement, the 5 experiments performed from 0.35 to 1.0 GPa show a minimum velocity at the expected temperature. $NA_{1.25}$ might suffer from overestimated temperature due to the proximity of melting temperature for halite at high pressure. In this latter experiment, unintentionally large temperature steps of 60 °C and 130 °C were performed for the last two heating steps within the α-field, while previous heating steps with equal heating power increment induced increments of about 10 °C only.

4.3 Velocities in the β-quartz field and possible experimental artefacts

Thermodynamic models generally account for the change of elastic properties at quartz $\alpha \rightarrow \beta$ transition, by propagating the elastic moduli measured at low pressure to high pressure (Angel et al., 2017; Abers & Hacker, 2016). In particular, Abers and Hacker (2016) use a null thermal expansion coefficient for the β-phase and extrapolate the fitting of low pressure K (isothermal bulk modulus) dependence on T at higher pressure, assuming dK/dP

to be equal to 4 in both the α- and the β- field. Consequently, the velocity jump they predict across the transition is unaffected by pressure change. P-wave velocities measured within α-field are in agreement with the ones predicted by Abers and Hacker (2016). However, our results seem to suggest that the amplitude of the increase in V_p through the $\alpha \rightarrow \beta$ transition decreases at increasing pressure. In the following, we discuss three possible causes for this discrepancy and the unexpected moderate velocities observed in the β-field: - transformation-induced cracks that might reduce V_p; ii- temperature gradients in the samples that could result in a progressive sample transformation; iii- potential errors when extrapolating the elastic parameters of β-quartz from low to high pressure, as already mentioned above.

Transformation-induced cracking
Cracking/fracturing at the transition temperature could modify the effective elastic behaviour at high pressure. At atmospheric pressure, experimental studies exhibit a peak of AEs at transition temperature (Schmidt-Mumm, 1991; Glover et al., 1995; Meredith et al., 2001). As previously discussed, no peak of acoustic emission has been observed near the transition temperature at 0.5 and 0.8 GPa on novaculite (Figure 5) which evidences that no major cracking affected our measurements. Although thermal expansion of quartz is anisotropic and varies through the $\alpha \rightarrow \beta$ phase transition, hence building up significant stress at grain boundaries, this effect is expected to be insignificant for grain sizes below 5 μm (McKnight et al., 2008). In addition, large pressure also should prevent mode-I cracking. So, both experimental results and mechanical considerations tend to discard this hypothetical artefact as a possible cause for the low velocities measured in the β-field.

Effects of temperature gradients
At room pressure, former studies have shown that the $\alpha \rightarrow \beta$ transformation occurs within a narrow temperature interval of < 1 °C. Considering that important temperature gradients are expected in our samples at high P-T (Moarefvand et al., 2021), the coexistence of the α and β phases is therefore likely over a temperature interval reflecting the range of temperature gradients, which, in turn, may explain why the present data does not exhibit a sharp velocity jump in the β-field with increasing temperature, but rather a steep continuous rebound. However, temperature gradients within the sample are estimated to be at most of a few tens of degrees (Moarefvand et al., 2021). These gradients alone can therefore not explain the low velocities obtained in the β)field, particularly in experiments $NA_{0.5}$and $NA_{0.8}$, where a good control on the temperature was kept far within the β-field ($\sim$100 °C), thus promoting full sample transformation. Temperature gradients inside the assembly lead, however, to transient mixed bulk elastic properties between untransformed low-velocity α domains and hotter transformed high-velocity β domains.

In order to evaluate the possible effect of temperature gradients, we modelled the evolution of P -wave velocities with Abers and Hacker (2016), considering a temperature gradient of - 50, - 100 and - 200 °C inside the sample assembly (Figure 14). A larger temperature gradient is expected to result in a less steep velocity change in both the α- and the β- quartz field (Figure 14). The slope of the velocity-temperature curve in the β- field from our experiment compares well with the increase computed for samples submitted to a gradient of 50-100 °C. On the other hand, the magnitude of the velocity decrease observed in the α- field is in agreement with (Abers & Hacker, 2016) predictions, which either suggests a negligible impact of temperature gradients in our samples, or reflects the gradual development of temperature gradients upon heating. Indeed, temperature gradients would lessen the decrease in velocity observed in the α-field, which is not observed. Nevertheless, heterogeneous transition within the sample would also imply heterogeneous transformational stress build-up, and hence heterogeneous Dauphiné twinning density. EBSD maps collected at the top versus that at the bottom, or at the core versus at the outer part of our samples, did not reveal any significant difference, suggesting that the transformation rate was rather homogeneous throughout each sample. Even though experimental artefacts might explain the observed limited velocity rise in the β-field, Johnson et al. (2021) numerical simulations show that the $\alpha \rightarrow \beta$ phase transition propagates due to heterogeneous stress distribution and quartz-grain orientations. Such a propagation mechanism over the timescale of our experiments cannot be excluded. However, no propagation pattern is observed in our EBSD maps (Fig. 9). Even the larger ones (up to 0.03 mm^2, figure 9) show homogeneous and isotropic twinning boundaries distributions, suggesting that, if occurring, this propagation was complete at peak temperatures. In summary, temperature gradients might well explain why the rise in velocity is less steep than predicted, but not why maximum velocities remain lower than that expected in the β-field.

Uncertainties regarding the elastic propoerties of β-quartz
Amongst the different equations of states or thermodynamic databases of quartz published in the literature, only the formalism of Dorogokupets (1995) predicts a decrease of the velocity rise within β-quartz with increasing pressure. Dorogokupets (1995) formalism also predicts that the λ-shaped anomaly spreads with increasing pressure and hence that the transition may become imperceptible at "some pressure", which is consistent with the imperceptible change in slope of the quartz-coesite transition at the intersection with the $\alpha \rightarrow \beta$ transition. This equation of state also implies that dK/dP is not constant in the β-field, and that it could even reach negative values at high pressures. Even though the actual physical meaning of a negative dK/dP remains unclear (at least to the authors of this manuscript), the comparison of our experimental results with V_p curves calculated with different dK/dP values using the (Abers & Hacker, 2016) formalism (Figure 14) suggests that this parameter might be indeed overestimated in most databases. For instance, using molar volume measurements, Lider and Yurtseven (2014) have calculated the isothermal compressibility of β-quartz as a quadratic function of P: $\kappa(P) = \kappa_o + \kappa_1 * P + \kappa_2 * P^2$, where κ_o and $\kappa(P)$ are the compressibilities of β-quartz at room pressure and at a given pressure, respectively. Using their coefficients ($\kappa_o = 0.035\ GPa^{-1}$; $\kappa_1 = -9.01 * 10^{-4}\ GPa^{-2}$; $\kappa_2 = -8.9 * 10^{-5}\ GPa^{-3}$) yields a bulk modulus of β quartz at room pressure and 1 GPa (and 878K) equal to 28.57 GPa and 29.4 GPa respectively, i.e. a dK/dP of ~ 0.8 only (close to the green dashed line in Figure 13).

5 Conclusions

We have investigated the α-β quartz transition at high pressure by measuring P-wave velocity with increasing temperature across the transition, at 0.35-1.25 GPa on both polycrystalline aggregates and single crystals. We observed a minimum in P-wave velocity at temperatures compatible with the predicted P-T conditions of the transition. The transition seems to occur at lower temperatures for single crystals than for the aggregates, which confirms an experimental observation by Kern (1978, 1979). We observe an increase in P-wave anisotropy with increasing pressure, P-wave velocities propagating 10-20% faster along the c-axis. P-wave anisotropy also decreases with increasing temperature in the α-quartz domain, and increases once in the β-quartz field.

Below the transition temperature, the expected softening, resulting in an important drop of the P-wave velocities, is well observed and matches the thermodynamic predictions. However, the increase of P-wave velocity within the β-quartz is smaller than predicted by thermodynamic databases (Figure 12), which is partly due, here, to the difficulties in investigating high temperatures with the use of NaCl as a pressure medium. Nevertheless, it is clearly observed that with increasing pressure, the velocity rise in the β-field becomes lower. Two experimental biases that can potentially explain this unexpected behavior were assessed: possible cracking through the transition and temperature gradients in the sample.

Acoustic emission monitoring revealed that there is no (dynamic) micro-cracking related to the transition, at least within the microcrystalline aggregate. Temperature gradients in the sample lead to gradual transformation of the sample, which explains the smoothing of the dip of the velocity-temperature curves at the transition compared to what is predicted by thermodynamics. However, the evolution of velocities in the α-quartz field compares very well with modelled velocity curves, which suggests a modest effect of thermal gradients on the transition. Whether or not these gradients remain small enough to allow full transformation beyond the minimum in velocity observed remains unclear. In other words, it is difficult to demonstrate that the highest velocity values obtained in the β-field actually do correspond to the maxima predicted by thermodynamics, which are supposed to be larger.

Dauphiné twins formed in all samples that underwent the $\alpha \rightarrow \beta$ transition and their homogeneous distribution across at least one of the samples points towards a full sample transformation. However, two samples show a twinning ratio comparable to that of the reference sample that remained in the α-quartz field (Table 2). It is therefore not possible to attribute all the twins to the transformation, and the respective contributions of grain-scale deviatoric stresses versus α-β transformation in producing Dauphiné twins remains to be determined.

Nevertheless, the increase of velocities obtained in the β-field becomes weaker with increasing pressure, which reveals that the bulk modulus of β-quartz and its pressure derivative remain largely unconstrained, and suggest that both K_o and K' are smaller than predicted by current thermodynamic databases. Consequently, the seismic anomaly related to the α-β quartz transition at high pressure might be smaller than predicted by these databases, which should thus be used with caution. Quartz grain size and orientation both can affect the transition temperature, and the elastic properties change due to the transition. In consequence, high pressure and temperature estimates of elastic parameters are still needed to improve the thermodynamic modelling of quartz, particularly within the β-quartz domain.

Finally, since the transition is expected to be smoother than currently computed, the above also implies a refinement of the interpretation of seismic discontinuities in terms of 'seismic signature' of the $\alpha \rightarrow \beta$ transition. While the K-horizon reflector documented in the Tuscany geothermal fields (Marini & Manzella, 2005) is shallow enough (9 km maximum, i.e. $\sim$ 0.3 GPa) to be directly due to the transition itself, the deeper reflectors at 15-20 km (ie 0.5 - 0.7 GPa) beneath Tibet (Mechie et al., 2004) or at 24 km (0.8 GPa) beneath Taïwan (Kuo-Chen et al., 2012) or even 50 km (1.7 GPa) beneath Southern Tibet (Sheehan et al., 2014) are less likely to be due to the position of the present-day transition. They could, however, be the signature in these now lowermost continental units of the irreversible damages caused by transition at lower pressure during burial. The use of this reflector as a present-day crustal geothermometer might therefore be less relevant at higher pressures.

6 Acknowledgement

This project was funded by the European Research Council grant REALISM (2016-grant 681346) led by A. Schubnel. We thank prof. Ross Angel for particularly constructive comments and discussions at the early stage of this study.

References

Abers, G. A., & Hacker, B. R. (2016). A matlab toolbox and e xcel workbook for calculating the densities, seismic wave speeds, and major element composition of minerals and rocks at pressure and temperature. *Geochemistry, Geophysics, Geosystems*, *17*(2), 616–624.

Angel, R. J., Alvaro, M., Miletich, R., & Nestola, F. (2017). A simple and generalised p–t–v eos for continuous phase transitions, implemented in eosfit and applied to quartz. *Contributions to Mineralogy and Petrology*, *172*(5), 29.

Bachmann, F., Hielscher, R., & Schaeben, H. (2010). Texture analysis with mtex–free and open-source software toolbox. In *Solid state phenomena* (Vol. 160, pp. 63–68).

Bagdassarov, N., & Delépine, N. (2004). α–β inversion in quartz from low frequency electrical impedance spectroscopy. *Journal of Physics and Chemistry of Solids*, *65*(8-9), 1517–1526.

Berman, R. G. (1988). Internally-consistent thermodynamic data for minerals in the system na2o-k2o-cao-mgo-feo-fe2o3-al2o3-sio2-tio2-h2o-co2. *Journal of petrology*, *29*(2), 445–522.

Birch, F. (1960). The velocity of compressional waves in rocks to 10 kilobars: 1. *Journal of Geophysical Research*, *65*(4), 1083–1102.

Birch, F. (1961). The velocity of compressional waves in rocks to 10 kilobars: 2. *Journal of Geophysical Research*, *66*(7), 2199–2224.

Carpenter, M. A., Salje, E. K., Graeme-Barber, A., Wruck, B., Dove, M. T., & Knight, K. S. (1998). Calibration of excess thermodynamic properties and elastic constant variations associated with the alpha¡–¿ beta phase transition in quartz. *American mineralogist*, *83*(1-2), 2–22.

Cohen, L. H., & Klement Jr, W. (1967). High-low quartz inversion: Determination to 35 kilobars. *Journal of Geophysical Research*, *72*(16), 4245–4251.

Darot, M., Gueguen, Y., Benchemam, Z., & Gaboriaud, R. (1985). Ductile-brittle transition investigated by micro-indentation: results for quartz and olivine. *Physics of the Earth and Planetary Interiors*, *40*(3), 180–186.

Doncieux, A., Stagnol, D., Huger, M., Chotard, T., Gault, C., Ota, T., & Hashimoto, S. (2008). Thermo-elastic behaviour of a natural quartzite: itacolumite. *Journal of materials science*, *43*(12), 4167–4174.

Dorogokupets, P. I. (1995). Equation of state for lambda transition in quartz. *Journal of Geophysical Research: Solid Earth*, *100*(B5), 8489–8499.

Gasc, J., Daigre, C., Moarefvand, A., Deldicque, D., Fauconnier, J., Gardonio, B., ... Schubnel, A. (2022). Deep-focus earthquakes: From high-temperature experiments to cold slabs. *Geology*, *50*(9), 1018–1022.

Gibert, B., & Mainprice, D. (2009). Effect of crystal preferred orientations on the thermal diffusivity of quartz polycrystalline aggregates at high temperature. *Tectonophysics*, *465*(1-4), 150–163.

Glover, P., Baud, P., Darot, M., Meredith, P., Boon, S., LeRavalec, M., ... Reuschlé, T. (1995). α/β phase transition in quartz monitored using acoustic emissions. *Geophysical Journal International*, *120*(3), 775–782.

Heaney, P. J., & Veblen, D. R. (1991). Observations of the α-β phase transition in quartz: a review of imaging and diffraction studies and some new results. *American mineralogist*, *76*(5-6), 1018–1032.

Holland, T., & Powell, R. (1998). An internally consistent thermodynamic data set for phases of petrological interest. *Journal of metamorphic Geology*, *16*(3), 309–343.

Holyoke III, C. W., & Kronenberg, A. K. (2010). Accurate differential stress measurement using the molten salt cell and solid salt assemblies in the griggs apparatus with applications to strength, piezometers and rheology. *Tectonophysics*, *494*(1-2), 17–31.

Johnson, S. E., Song, W. J., Cook, A. C., Vel, S. S., & Gerbi, C. C. (2021). The quartz α β phase transition: Does it drive damage and reaction in continental crust? *Earth and Planetary Science Letters*, *553*, 116622.

Kern, H. (1978). The effect of high temperature and high confining pressure on compressional wave velocities in quartz-bearing and quartz-free igneous and metamorphic rocks. *Tectonophysics*, *44*(1-4), 185–203.
Kern, H. (1979). Effect of high-low quartz transition on compressional and shear wave velocities in rocks under high pressure. *Physics and Chemistry of Minerals*, *4*(2), 161–171.
Kuo-Chen, H., Wu, F., Jenkins, D., Mechie, J., Roecker, S., Wang, C.-Y., & Huang, B.-S. (2012). Seismic evidence for the α-β quartz transition beneath taiwan from vp/vs tomography. *Geophysical Research Letters*, *39*(22).
Le Chatelier, H. (1890). Sur la dilatation du quartz. *Bulletin de Minéralogie*, *13*(3), 112–118.
Lider, M., & Yurtseven, H. (2014). α-β transition in quartz: Temperature and pressure dependence of the thermodynamic quantities for β-quartz and β-cristobalite as piezoelectric materials. *3D Research*, *5*(4), 1–9.
Mainprice, D., & Casey, M. (1990). The calculated seismic properties of quartz mylonites with typical fabrics: relationship to kinematics and temperature. *Geophysical Journal International*, *103*(3), 599–608.
Marini, L., & Manzella, A. (2005). Possible seismic signature of the α–β quartz transition in the lithosphere of southern tuscany (italy). *Journal of volcanology and geothermal research*, *148*(1-2), 81–97.
McGinn, C., Miranda, E. A., & Hufford, L. J. (2020). The effects of quartz dauphiné twinning on strain localization in a mid-crustal shear zone. *Journal of Structural Geology*, *134*, 103980. Retrieved from `https://www.sciencedirect.com/science/article/pii/S0191814118304851` doi: https://doi.org/10.1016/j.jsg.2020.103980
McKnight, R. E., Moxon, T., Buckley, A., Taylor, P., Darling, T., & Carpenter, M. (2008). Grain size dependence of elastic anomalies accompanying the α–β phase transition in polycrystalline quartz. *Journal of Physics: Condensed Matter*, *20*(7), 075229.
Mechie, J., Sobolev, S. V., Ratschbacher, L., Babeyko, A. Y., Bock, G., Jones, A., ... Zhao, W. (2004). Precise temperature estimation in the tibetan crust from seismic detection of the α-β quartz transition. *Geology*, *32*(7), 601–604.
Meredith, P. G., Knight, K. S., Boon, S. A., & Wood, I. G. (2001). The microscopic origin of thermal cracking in rocks: An investigation by simultaneous time-of-flight neutron diffraction and acoustic emission monitoring. *Geophysical research letters*, *28*(10), 2105–2108.
Minor, A., Rybacki, E., Sintubin, M., Vogel, S., & Wenk, H.-R. (2018). Tracking mechanical dauphiné twin evolution with applied stress in axial compression experiments on a low-grade metamorphic quartzite. *Journal of Structural Geology*, *112*, 81-94. Retrieved from `https://www.sciencedirect.com/science/article/pii/S0191814118301937` doi: https://doi.org/10.1016/j.jsg.2018.04.002
Mirwald, P. W., & Massonne, H.-J. (1980). The low-high quartz and quartz-coesite transition to 40 kbar between 600° and 1600° c and some reconnaissance data on the effect of naalo2 component on the low quartz-coesite transition. *Journal of Geophysical Research: Solid Earth*, *85*(B12), 6983–6990.
Moarefvand, A., Gasc, J., Fauconnier, J., Baïsset, M., Burdette, E., Labrousse, L., & Schubnel, A. (2021). A new generation griggs apparatus with active acoustic monitoring. *Tectonophysics*, 229032.
Nikitin, A., Vasin, R., Balagurov, A., Sobolev, G., & Ponomarev, A. (2006). Investigation of thermal and deformation properties of quartzite in a temperature range of polymorphous α-β transition by neutron diffraction and acoustic emission methods. *Physics of Particles and Nuclei Letters*, *3*(1), 46–53.
Ohno, I. (1995). Temperature variation of elastic properties of α-quartz up to the α-β transition. *Journal of Physics of the Earth*, *43*(2), 157–169.
Ohno, I., Harada, K., & Yoshitomi, C. (2006). Temperature variation of elastic constants of quartz across the α-β transition. *Physics and Chemistry of Minerals*, *33*(1), 1–9.
Schmidt-Mumm, A. (1991). Low frequency acoustic emission from quartz upon heating

from 90 to 610 c. *Physics and Chemistry of Minerals*, *17*(6), 545–553.

Sheehan, A. F., de la Torre, T. L., Monsalve, G., Abers, G. A., & Hacker, B. R. (2014). Physical state of himalayan crust and uppermost mantle: Constraints from seismic attenuation and velocity tomography. *Journal of Geophysical Research: Solid Earth*, *119*(1), 567–580.

Shen, A., Bassett, W., & Chou, I.-M. (1993). The α-β quartz transition at high temperatures and pressures in a diamond-anvil cell by laser interferometry. *American Mineralogist*, *78*(7-8), 694–698.

Van Groos, A. K., & Heege, J. T. (1973). The high-low quartz transition up to 10 kilobars pressure. *The Journal of Geology*, *81*(6), 717–724.

Wenk, H.-R., Barton, N., Bortolotti, M., Vogel, S., Voltolini, M., Lloyd, G., & Gonzalez, G. (2009). Dauphiné twinning and texture memory in polycrystalline quartz. part 3: texture memory during phase transformation. *Physics and Chemistry of Minerals*, *36*(10), 567–583.

Wenk, H.-R., Rybacki, E., Dresen, G., Lonardelli, I., Barton, N., Franz, H., & Gonzalez, G. (2006). Dauphiné twinning and texture memory in polycrystalline quartz. part 1: experimental deformation of novaculite. *Physics and Chemistry of Minerals*, *33*, 667–676.

Zappone, A. S., & Benson, P. M. (2013). Effect of phase transitions on seismic properties of metapelites: A new high-temperature laboratory calibration. *Geology*, *41*(4), 463–466.

Exp. n	Sample	Method	$P_c(GPa)$	$L_0(mm)$	$L_f(mm)$	$T_{\alpha \to \beta}(^{\circ}C)$	Duration (min)
$NA_{0.35}$	Novaculite	active	0.35	10.1	9.48	661	46
$NA_{0.5}$	Novaculite	active	0.5	10.5	9.7	720	57
$NA_{0.65}$	Novaculite	”	0.65	10.3	10.2	753	112
$NA_{0.8}$	Novaculite	”	0.8	10.39	9.9	770	150
$NA_{0.9}$	Novaculite	”	0.9	9.3	9	766	78
NA_1	Novaculite	”	1	10.4	10.3	781	107
NA_1^*	Novaculite	”	1	9.6	9.4	–	–
$NA_{1.25}$	Novaculite	”	1.25	10.1	9.9	824	97
$NP_{0.5}$	Novaculite	passive	0.5	10.94	10.1	–	71
$NP_{0.8}$	Novaculite	”	0.8	11	10.3	–	120
$SA_{0.5a}$	S.C a-axis	active	0.5	11	10.8	720	86
$SA_{0.5c}$	S.C c-axis	”	0.5	10.1	10.0	695	53
$SA_{0.8a}$	S.C a-axis	”	0.8	11	10.4	750	100
$SA_{0.8c}$	S.C c-axis	”	0.8	10.9	10.3	742	81

Table 1. Summary of experimental conditions. The transition temperature refers to the conditions where the minimum in P-wave velocity was detected. The experimental duration refers to the time at high pressure during which the temperature was increased. Abbreviations: N for Novaculite, S for Single-crystal, A for active and P for passive acoustic monitoring. $*$ Contrary to NA_1 and all of the other experiments, this one remained in the α-quartz field.

Sample	Number of EBSD maps	Mean grain size (μm)	Mean aspect ratio	Mean shape factor	Mean Twin. Ratio %	Deviation. %
Starting material	1	5.51	1.34	1.44	0.40	—
$NA_{0.5}$	3	4.08	1.47	1.66	19.2	3.3
$NA_{0.65}$	9	4.41	1.53	1.45	6.30	0.7
$NA_{0.8}$	3	3.50	1.42	1.56	19.2	3.4
NA_{1}	3	4.34	1.47	1.53	18.7	0.3
$NA_{1.25}$	9	4.00	1.63	1.46	8.90	3.6
NA_{1}^{*}	2	4.86	1.37	1.46	8.00	0.8

Table 2. Result of EBSD analysis of starting material (Novaculite), sample of experiments on novaculite. Grain size is in μm. Twinning ratio is the total length of Dauphiné twin boundaries over the total length of grain boundaries. The two rightmost columns give the mean value of the twinning ratio its standard deviation. Experiment NA_1^* remained in the α-quartz field and didn't cross the transition.

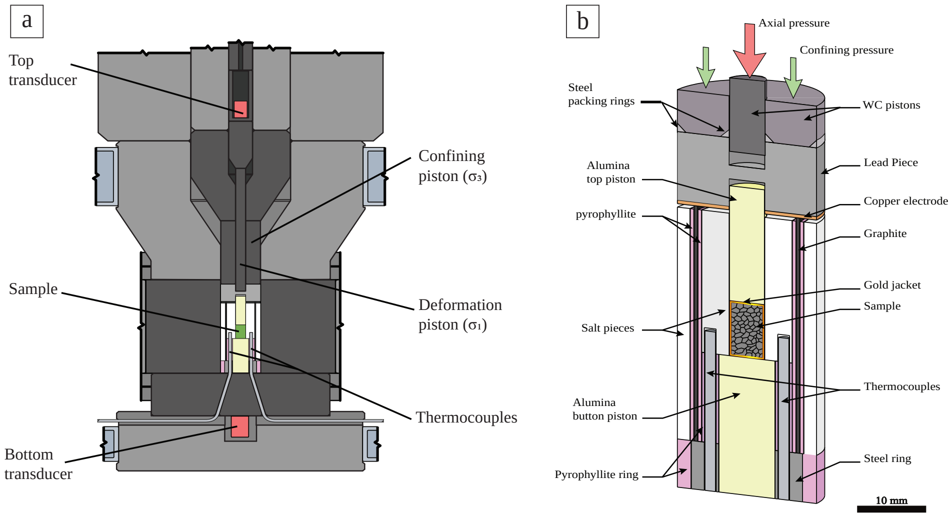

Figure 1. (a) Vertical cross-section of the sample assembly. (b) Schematics of the *Griggs* set-up with the position of the sample assembly and of the ultrasonic transducers.

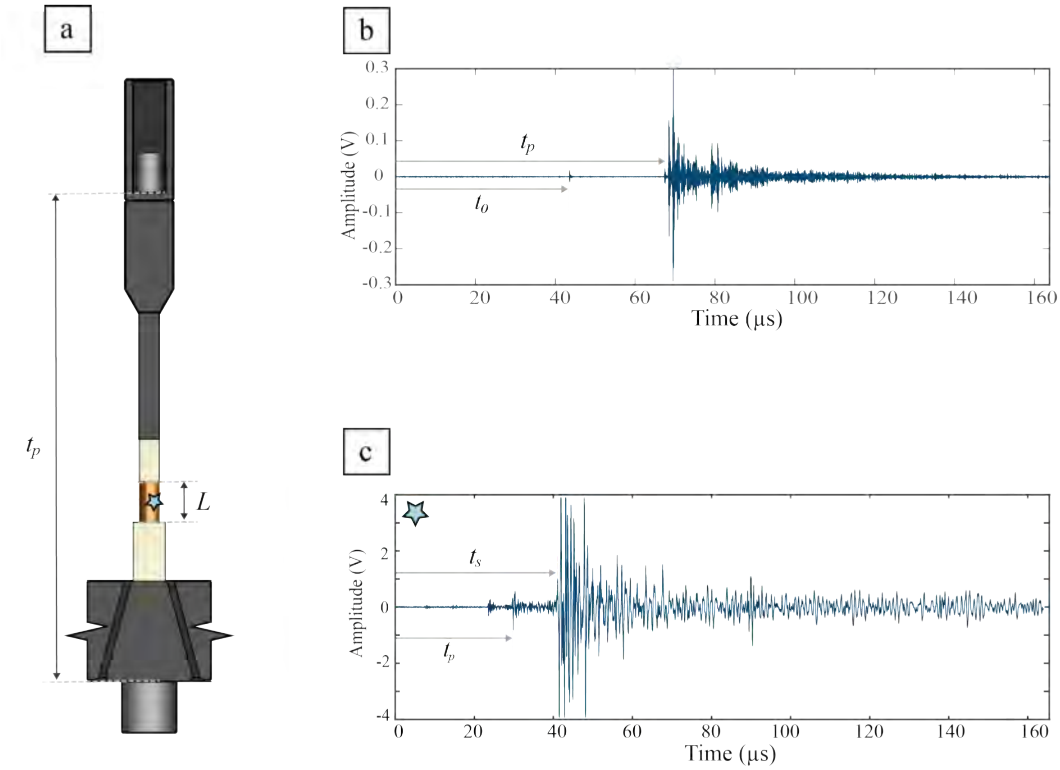

Figure 2. (a) Acoustic monitoring set-up. t_p is the travel time between the two transducers and L the sample length (b) Typical waveform recorded by the top transducer during a velocity survey. t_o is the time at which the pulse is sent to the bottom transducer. (c) Typical waveform of an acoustic emission generated inside the sample and recorded by bottom transducer, amplified at 60 dB and high-pass filtered above 500 KHz.

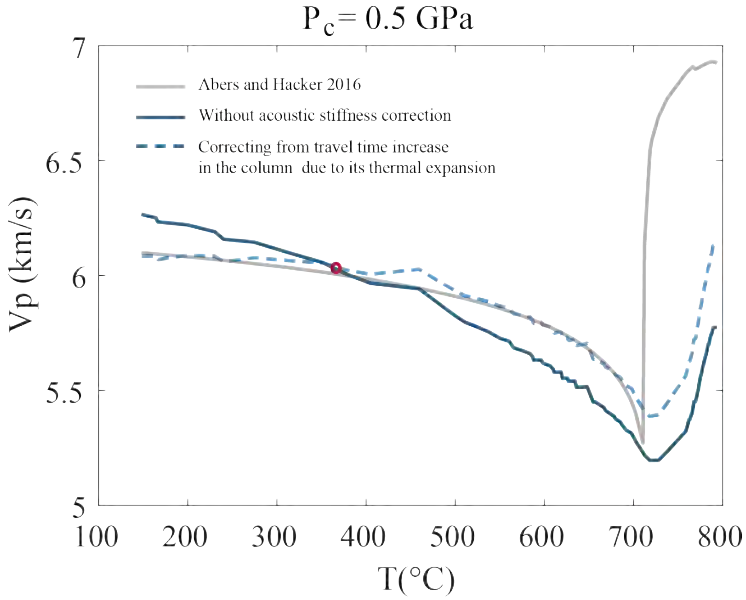

Figure 3. P wave velocity (V_p) versus temperature. The gray solid line represents V_p calculated using (Abers & Hacker, 2016) code at experimental pressure and temperature conditions. The blue solid and dashed lines represent V_p calculated from arrival times, with (dashed line) and without (solid line) correcting the travel-times from the thermal expansion of the loading column. $V_p(0.5GPa, 350^oC)$ (red dot) is our anchor point, which was set to match (Abers & Hacker, 2016)'s prediction.

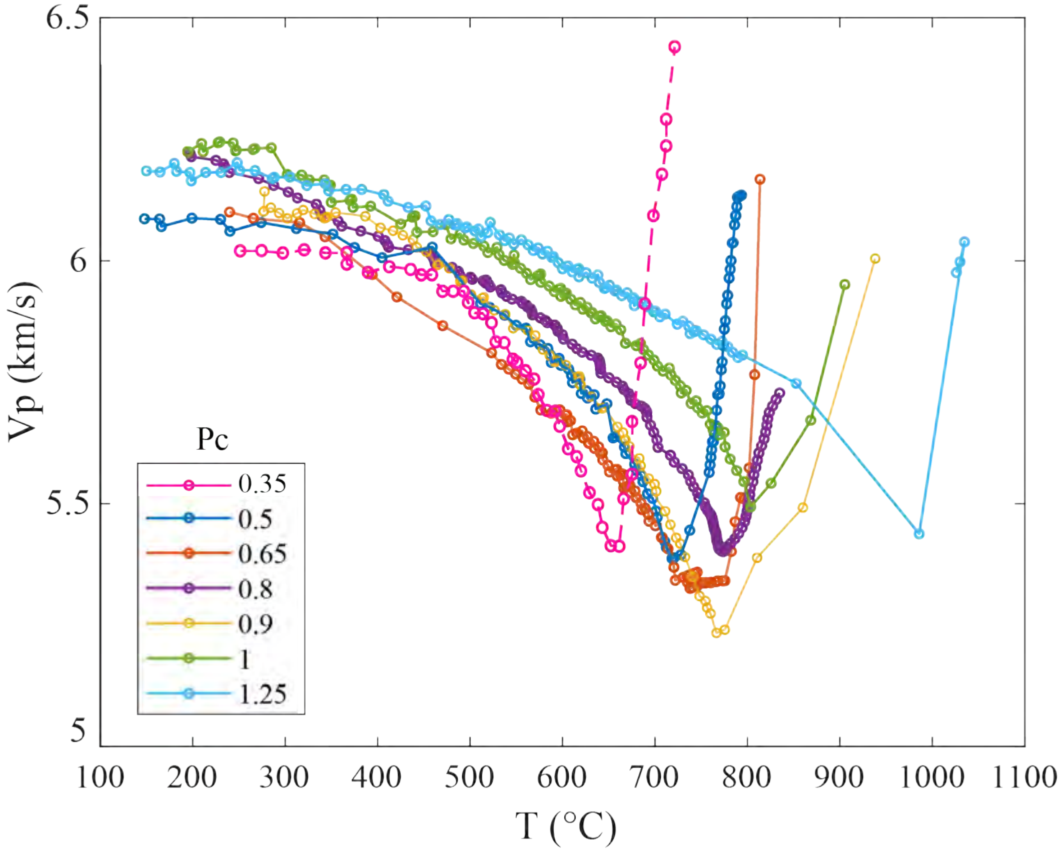

Figure 4. P wave velocity (V_p) versus temperature for confining pressure ranging from 0.35 to 1.25 GPa. Velocities were calculated relative to a reference point at 350°C (gray solid line, see section 2.4 for details).

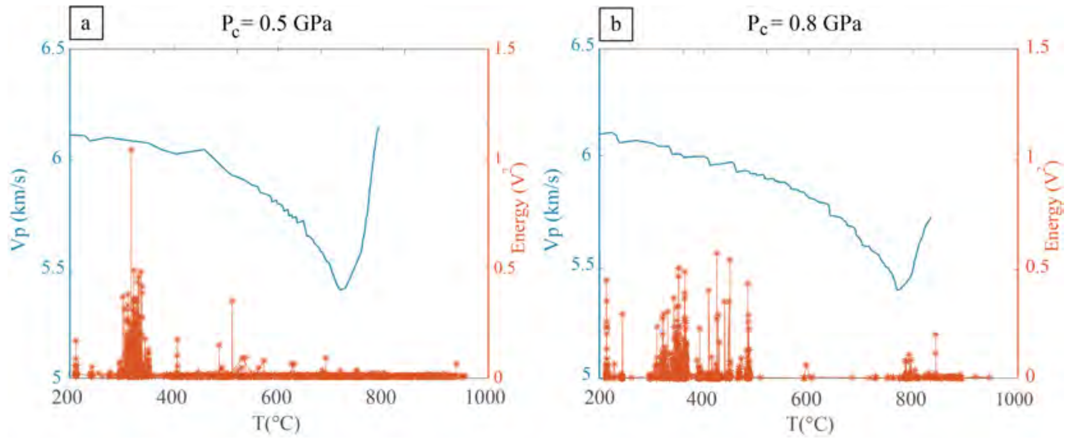

Figure 5. P wave velocity (left blue axis) and acoustic emission energy (right red axis) versus temperature at (a) 0.5 GPa and (b) 0.8 GPa confining pressure. Each star represents an acoustic emission. Note that each subplot also displays two different experiments ($NA_{0.5}$ and $NP_{0.5}$ 0.5 GPa and $NA_{0.8}$ and $NP_{0.8}$ at 0.5 GPa) since our current system does not allow doing both active and passive acoustic monitoring concurrently.

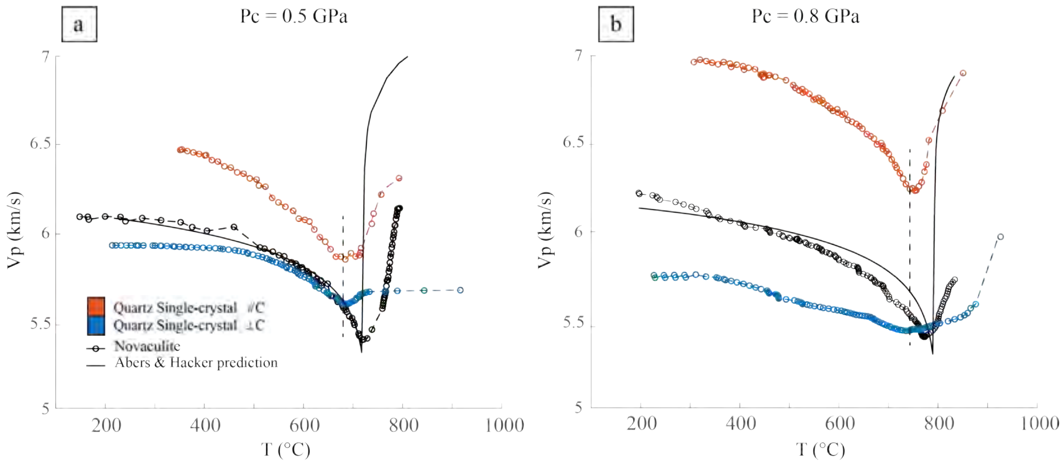

Figure 6. P wave velocities in novaculite versus quartz single crystal. Black solid lines represent the prediction of Abers and Hacker (2016), black circles are the present data obtained on Novaculite, red and blue circles are from single crystal c-axis-parallel and -perpendicular measurements, respectively. (a) 0.5 GPa (experiments $SA_{0.5a}$ and $SA_{0.5c}$) and (b) 0.8 GPa (experiments $SA_{0.8a}$ and $SA_{0.8c}$)

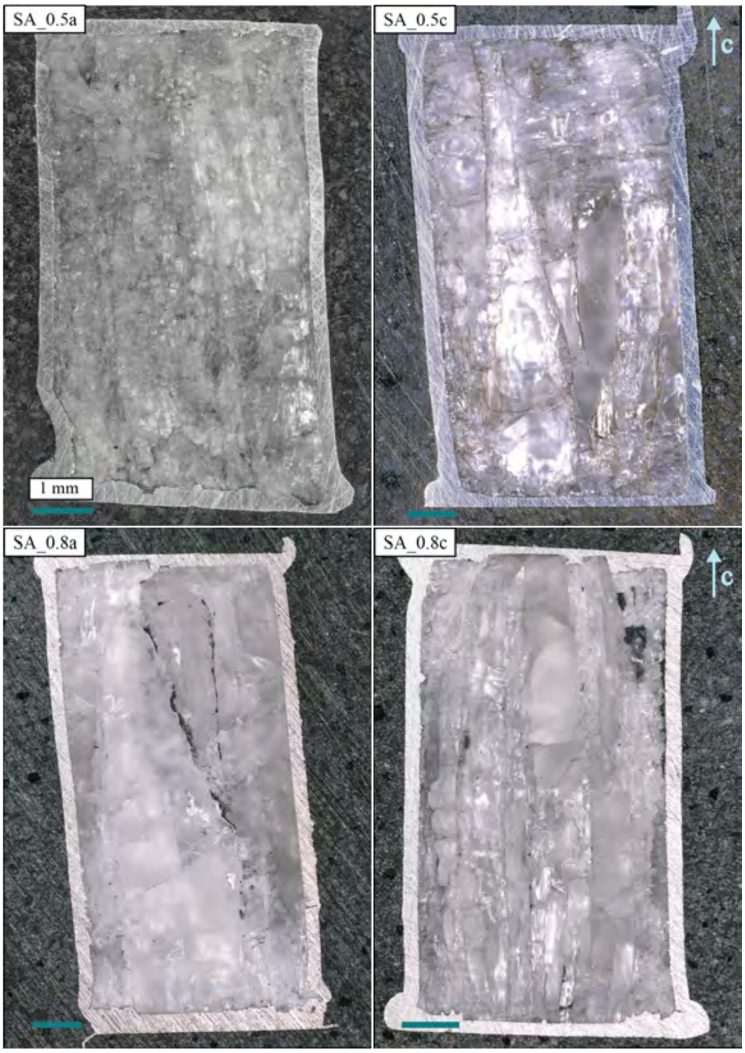

Figure 7. Images of quartz single-crystal samples from experiments at 0.5 and 0.8 GPa. Samples were cored parallel to c-axis and the other two perpendicular to c-axis, as indicated in the top right corner of each image. Scale bar is 1 mm long on all images. The vertical and horizontal cracks are not present in the samples prior to the experiment; their origin is discussed in section 3.3

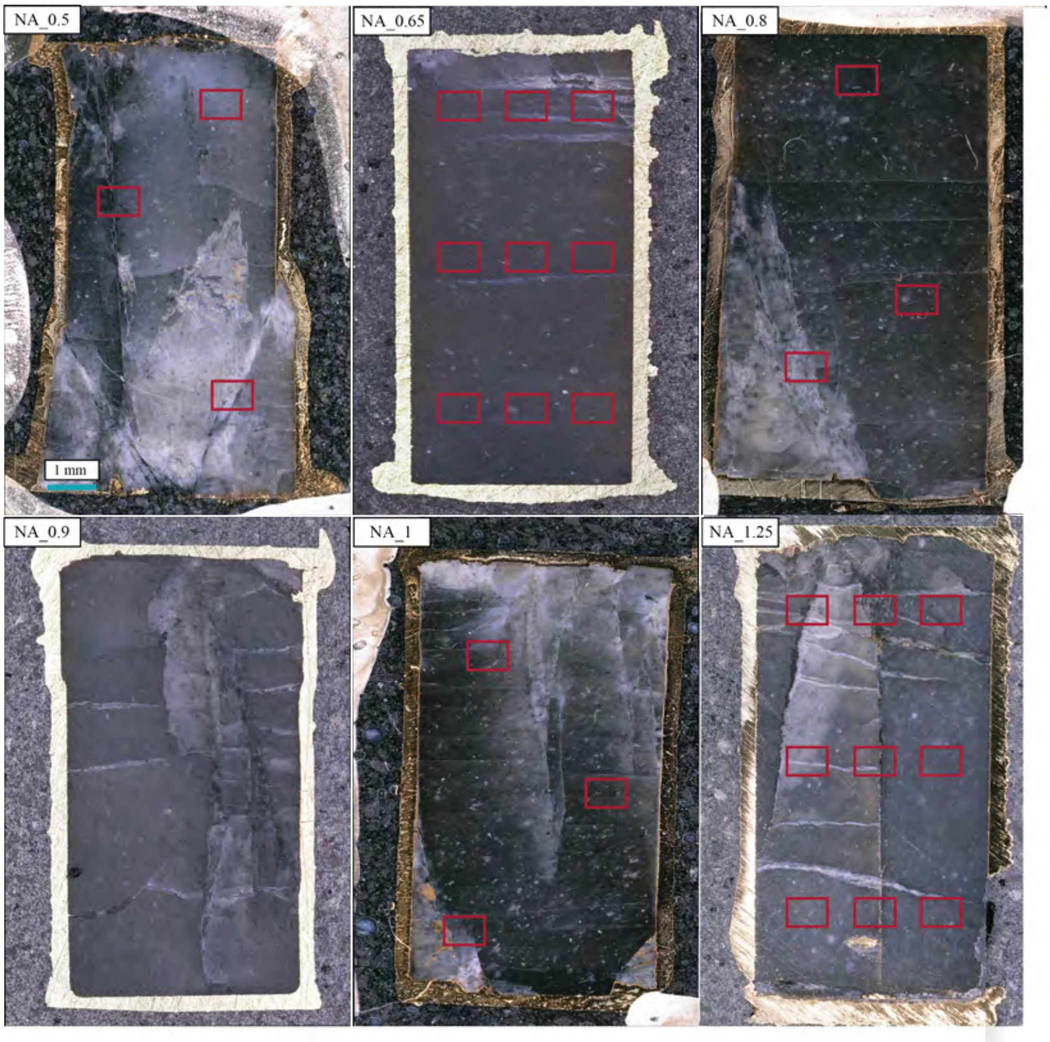

Figure 8. Images of Novaculite samples from experiments at 0.5, 0.65, 0.8, 0.9, 1 and 1.25 GPa. Red rectangles represent zones with EBSD analyses.

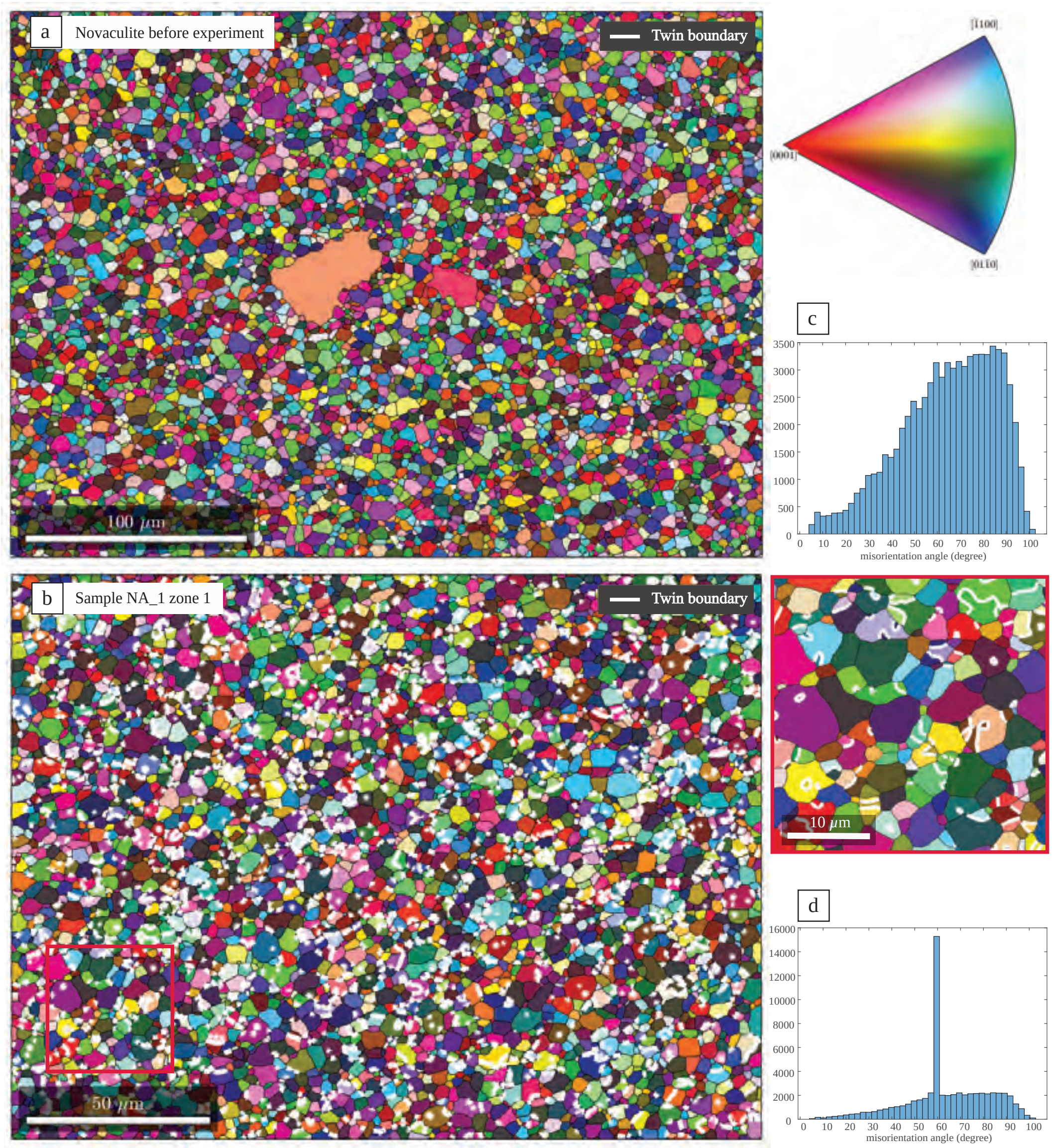

Figure 9. Electron Back Scatter Diffraction (EBSD) image of (a) the novaculite starting material and (b) sample of experiment NA_1 at 1 GPa. White lines represent Dauphiné twin boundaries. (c) and (d) are histograms of novaculite grain misorientations for maps shown in (a) and (b), respectively. The red rectangle on the right shows a magnified view according to the rectangle in (b).

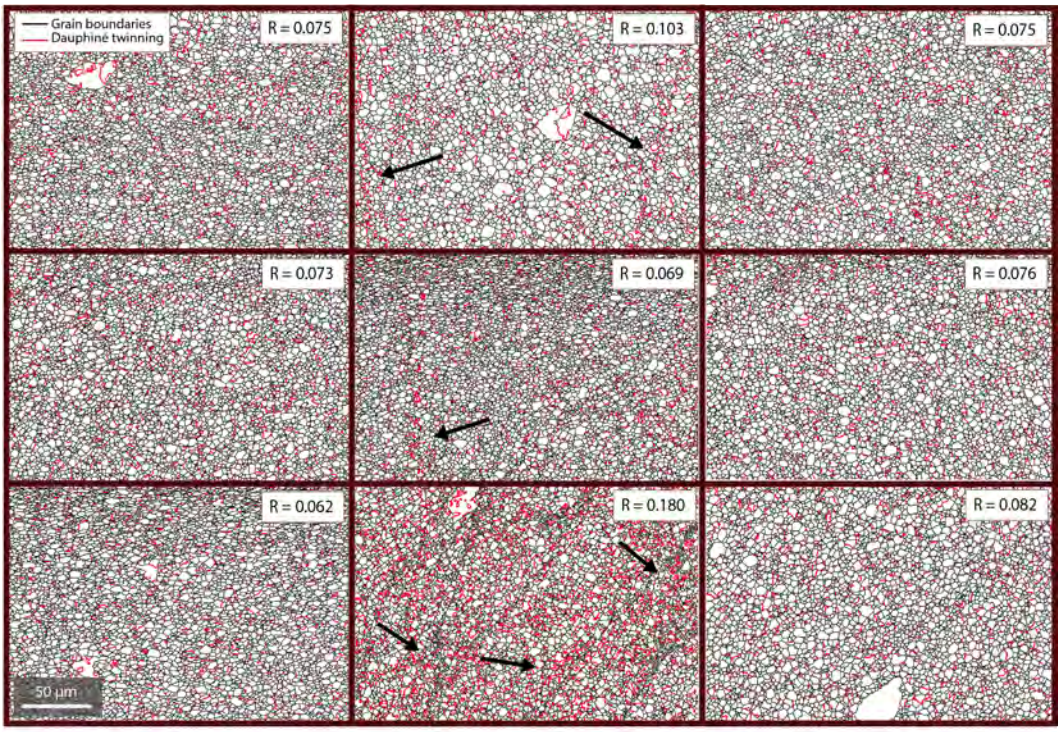

Figure 10. Dauphiné twin boundaries calculated from EBSD images on sample $NA_{1.25}$. R is the twinning ratio. Cracks, which display a higher density of twins are pointed out by arrows.

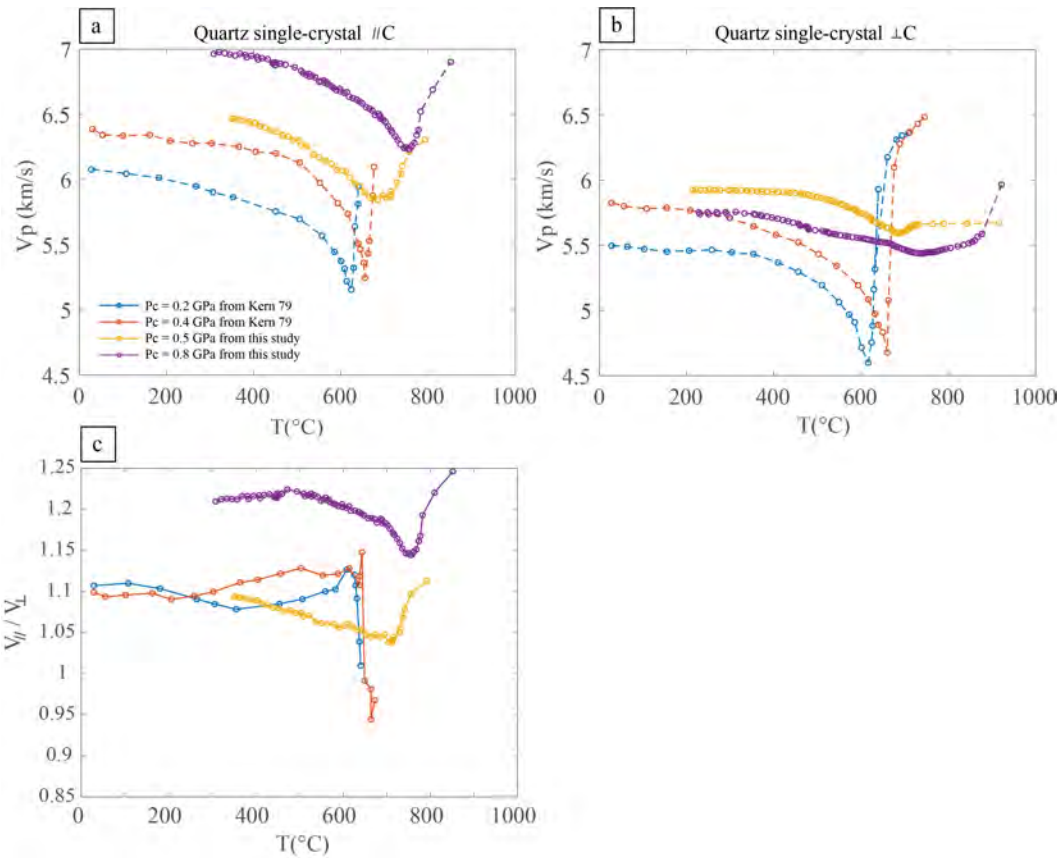

Figure 11. P-wave velocity in quartz single crystals versus temperature (a) $V_{\parallel c}$ along the c-axis, (b) $V_{\perp c}$ along the a-axis, and (c) P-wave anisotropy $V_{\parallel}/V_{\perp}$. The yellow and purple curves represent data obtained at 0.5 and 0.8 GPa, respectively. The blue and red curves represent experimental data from (Kern, 1979) at 0.2 and 0.4 GPa, respectively.

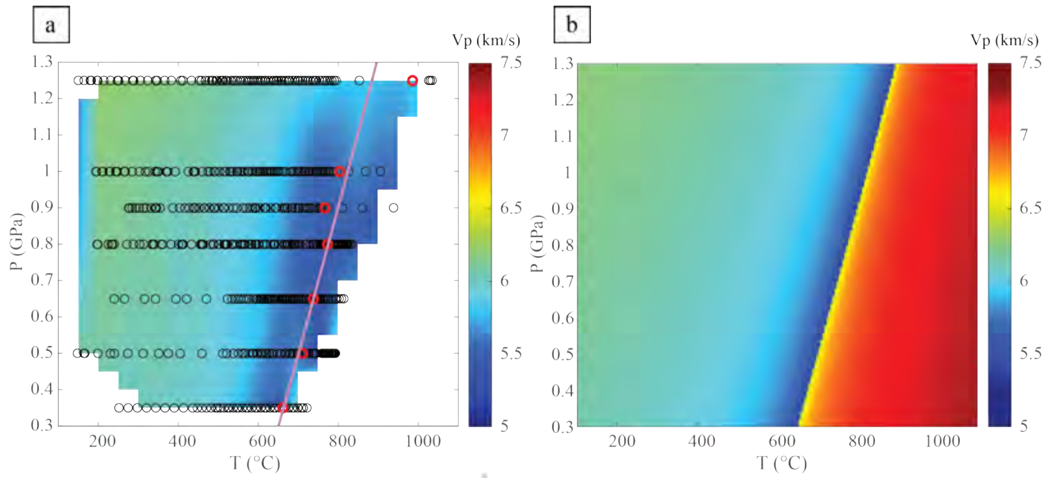

Figure 12. (a) P-wave velocity of quartz as a function of pressure and temperature. P-T conditions for $\alpha \rightarrow \beta$ transition (black solid line) is from (Shen et al., 1993). a) interpolation of experimentally derived P-wave velocities. Black circles correspond to data points; red circles to the P-T conditions at which the minimum P-wave velocity was observed of each experiment, the gray data point represents the reference point (see 2.4). (b) P-wave velocity prediction from (Abers & Hacker, 2016). The colorbar is the same for both panels.

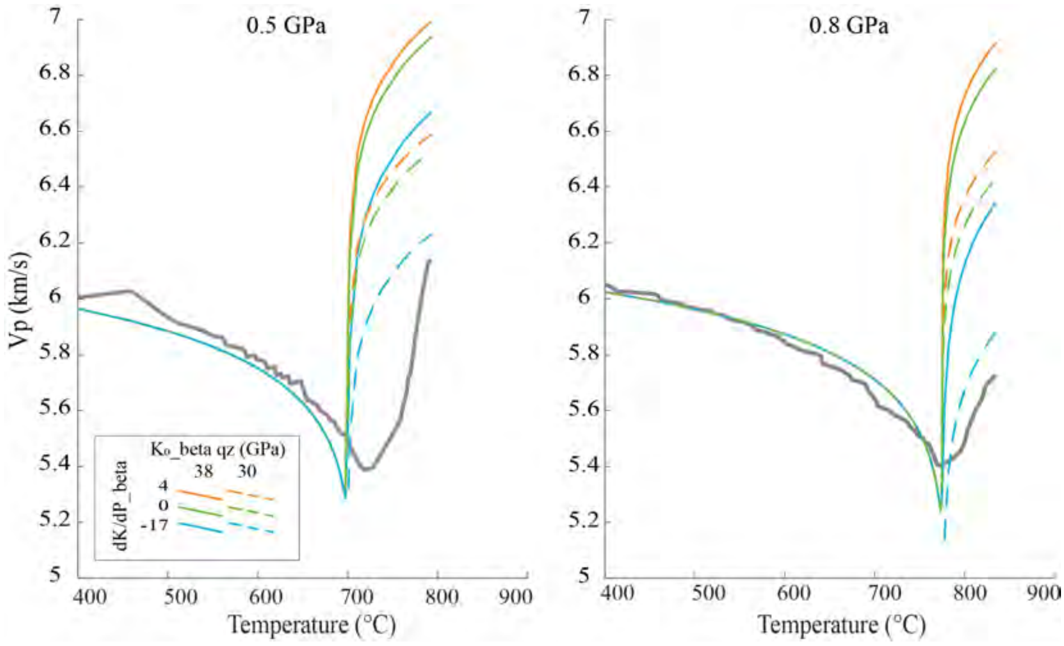

Figure 13. P wave velocity versus temperature at 0.5 GPa (left) and 0.8 GPa (right). Black circles represent our experimental data, black solid line represents the prediction of Abers and Hacker (2016) at experimental pressure and temperature conditions (i.e., with no temperature gradient). Blue, orange and red line are calculated from (Abers & Hacker, 2016) code assuming linear temperature gradients of -50C, -100C and -200C inside the sample.

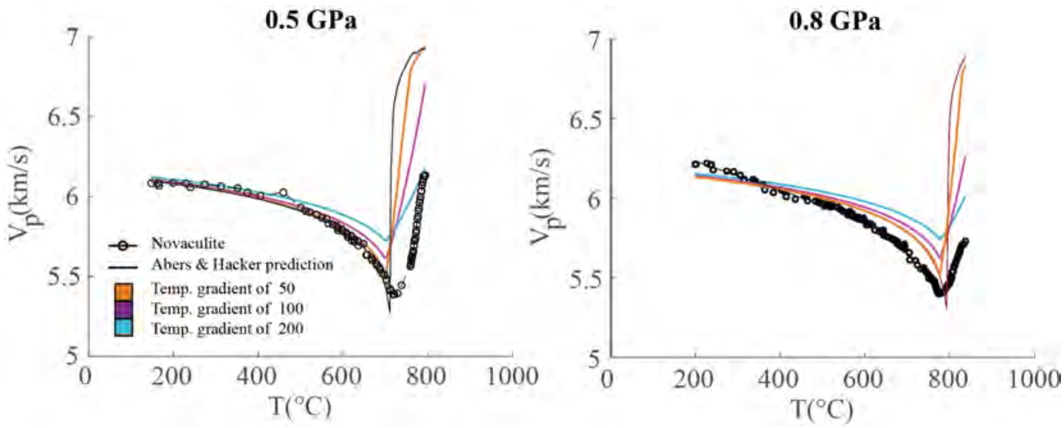

Figure 14. P-wave velocity vs temperature for different values of K_o and $K'(= dK/dP)$ for β quartz. Left, 0.5 GPa; right, 0.8 GPa. Gray solid lines represent data points obtained in this study. Solid and dashed lines are calculations with room pressure bulk moduli of $K_o = 38$ GPa and $K_o = 30$ GPa, respectively. Orange, green and blue curves represent calculations for K' equal to of 4, 0, and -17 respectively.